Coupled Lines for Wearable Power Dividers

Hee-Ran Ahn,
Manos M. Tentzeris,
Tong-Hong Lin, Bijan Tehrani,
and Xuanke He

In 2013, the Global Standards Initiatives on Internet of Things (IoT) defined the IoT as "a global infrastructure for the information society, enabling advanced services by interconnecting things based on existing and evolving interoperable information and communication technologies," with the term "thing" described as an object in the information world that is capable of being indentified and integrated into communication networks. Things in the IoT sense can, therefore, refer to a wide variety of devices for media, environmental monitoring, infrastructure management, manufacturing, energy management, medicine and health care, building and home automation, transportation, metropolitan-scale deployments, and consumer applications that demand accurate and reliable methods to sense changes, even in extremely rugged environments [1].

Power dividers that commonly use coupled transmission lines (CPLs), including directional couplers for arbitrary division ratios, are critical for most IoT modules, especially in wearable and flexible RF applications. The first directional coupler was reported in 1922 [2], and significant progress was made through the 1940s and 1950s [3], [4]. During the 1960s and 1970s, numerous papers [5]–[12] extended the theory, and various applications and developments have been continuously reported since then [13]–[27].

Two-port CPLs may be obtained by terminating two ports of a four-port directional coupler in open/short

Hee-Ran Ahn (hranahn@gmail.com), Manos M. Tentzeris (etentze@ece.gatech.edu), Tong-Hong Lin (thlin@gatech.edu), Bijan Tehrani (btehrani3@gatech.edu), and Xuanke He (xhe53@gatech.edu) are with the School of Electrical and Computer Engineering, Georgia Institute of Technology, Atlanta.

circuits in a diagonal fashion, but, if the conventional design formulas are applied, they can be perfectly matched for only the coupling coefficients of −3 dB. The realization of −3-dB coupling coefficients with microstrip technologies does not seem to be easy in numerous planar structures due to the dominant quasi-transverse-electromagnetic mode of the microstrip CPLs. In addition, perfect matching for arbitrary power ratios is necessary for numerous practical applications and, therefore, requires conventional design formulas to be modified. Two-port CPLs can feature special properties that single transmission lines (TLs) cannot possess, thus leading to their increasing use in a diverse set of RF applications, such as wideband ring hybrids [19], [28]–[32], dc blocks [33]–[36], compact and wideband dc blocks [20], Marchand baluns [37]–[41], high-impedance TLs [19], [27], [42], [44], [45], Wilkinson and Gysel power dividers with high power-division ratios [15], [16], and ring and branch-line hybrids with high power-division ratios [19], [32], [44]. This article discusses, in detail, four-port directional couplers and their compact equivalent circuits and how to modify the conventional design formulas of two-port CPLs and apply the modified design formulas for planar implementation and the miniaturization of various RF circuit topologies of power dividers using CPLs as building blocks.

The Directional Coupler and Its Compact and Wideband Equivalent Circuits

A directional coupler terminated in equal impedances Z_0 is depicted in Figure 1(a), where ports 1, 2, 3, and 4 and the even- and odd-mode impedances of Z_{0e} and Z_{0o} are indicated [18]. When the directional coupler is 90° long at the design frequency, the CPL is perfectly matched for a coupling coefficient of C. When unity power is excited at port 1, the power of $1 − C^2$ is delivered to port 4, and the rest of the power, C^2, is coupled to port 3, while port 2 is perfectly isolated. The design formulas for the even- and odd-mode impedances are given as

$$Z_{0e} = Y_{0e}^{-1} = Z_0 \sqrt{\frac{1+C}{1-C}}, \; Z_{0o} = Y_{0o}^{-1} = Z_0 \sqrt{\frac{1-C}{1+C}}, \quad (1)$$

where Z_0 and C are the termination impedance and the design coupling coefficient, respectively.

When $C = −3$ dB (0.707), the frequency responses are as plotted in Figure 2. All of the scattering parameters
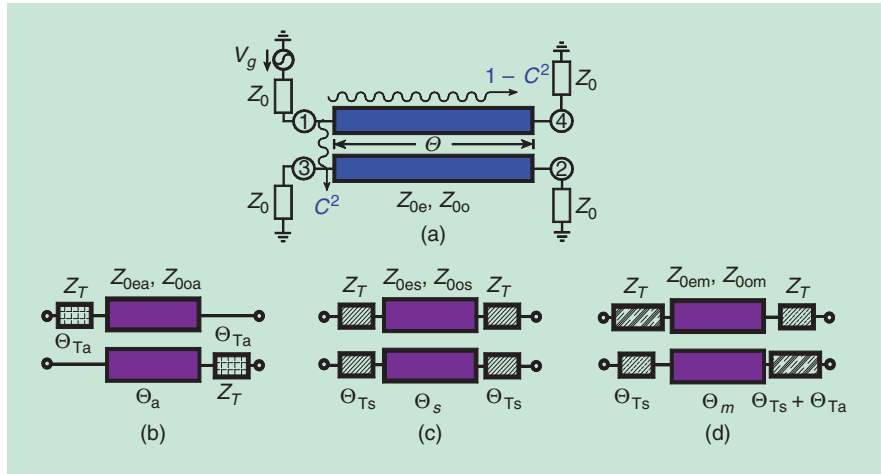

Figure 1. *The directional coupler and its compact and wideband equivalent circuits. (a) The directional coupler, (b) asymmetric equivalent circuit, (c) symmetric equivalent circuit, and (d) mixed equivalent circuit.*
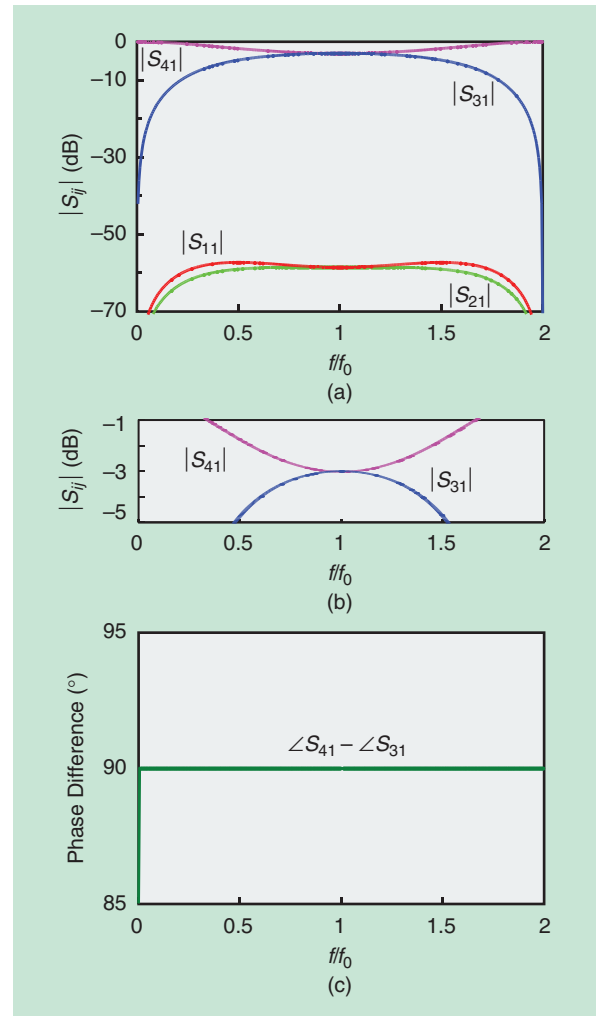

Figure 2. *The frequency responses of the directional coupler. (a) The scattering parameters. (b) A close view of the power division of $|S_{41}|$ and $|S_{31}|$. (c) The phase difference between $\angle S_{41}$ and $\angle S_{31}$.*

are shown in Figure 2(a) and (b), while the phase difference between the two scattering parameters of $\angle S_{41}$ and $\angle S_{31}$ is shown in Figure 2(c), where f and f_0 are the operating and design frequencies, respectively. The two frequency responses of S_{41} and S_{31} meet only at f_0 with the value of -3 dB, and very wideband matching and isolation can be achieved as shown in Figure 2(a). The phase difference between $\angle S_{41}$ and $\angle S_{31}$ is 90° regardless of the frequency, which is why directional couplers can be used for various applications. Asymmetric, symmetric, and mixed equivalent circuits with single TLs are suggested in Figure 1(b)–(d), respectively, to increase the bandwidth of the directional couplers and implement a Marchand balun in planar structures.

TABLE 1. The design parameters for Z_{0ea}, Z_{0oa}, and Θ_a in an asymmetric equivalent circuit for $Z_{0e} = 120.9$ Ω and $Z_{0o} = 20.7$ Ω, with a -3-dB coupling coefficient.

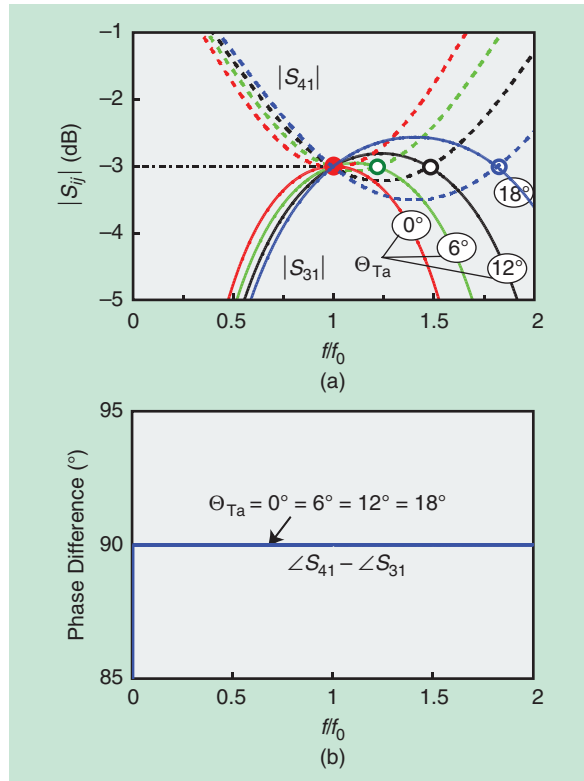| Θ_{Ta}	Z_{0ea} (Ω)	Z_{0oa} (Ω)	Θ_a (°)
0°	120.9	20.7	90
3°	121.15	20.64	85.75
6°	121.87	20.51	81.49
9°	123.1	20.31	77.2
12°	124.9	20.02	72.88

Figure 3. *The frequency responses of the asymmetric equivalent circuit in Figure 1(b). (a) $|S_{31}|$ and $|S_{41}|$. (b) The phase difference of $\angle S_{41} - \angle S_{31}$.*

The equivalent circuits can contribute to connecting segments between two directional couplers in a Marchand balun.

Asymmetric Equivalent Circuit

The proposed asymmetric equivalent circuit in Figure 1(b) consists of one CPL with arbitrary electrical length Θ_a and two identical uncoupled TLs connected to two ports of the coupled-line topology in a diagonal fashion. The characteristic impedances and electrical lengths of the uncoupled TLs are $Z_T = Y_T^{-1} = \sqrt{Z_{0e}Z_{0o}}$ and Θ_{Ta}, respectively, while the even- and odd-mode characteristic impedances and electrical length of the CPL are Z_{0ea}, Z_{0oa}, and Θ_a, respectively. The design formulas for the asymmetric circuit [18] are given as

$$\cos\Theta_a = \frac{T_{22}(Y_T^2 - A_{13}^2)}{T_{11}T_{21}A_{14}}, \tag{2a}$$

$$Y_{0ea} = Z_{0ea}^{-1} = j\left(\frac{T_{11}T_{21}A_{14}}{T_{11}^2 - A_{13}^2} - \frac{T_{12}^2 A_{13}}{T_{11}^2 - A_{13}^2}\right)\sin\Theta_a, \tag{2b}$$

$$Y_{0oa} = Z_{0oa}^{-1} = j\left(\frac{T_{11}T_{21}A_{14}}{T_{11}^2 - A_{13}^2} + \frac{T_{12}^2 A_{13}}{T_{11}^2 - A_{13}^2}\right)\sin\Theta_a, \tag{2c}$$

where

$A_{13} = j(Y_{0e} - Y_{0o})/2$, $A_{14} = j(Y_{0e} + Y_{0o})/2$, $T_{11} = T_{22} = jY_T\cot\Theta_{Ta}$ and $T_{12} = T_{21} = -jY_T\csc\Theta_{Ta}$.

Based on the formulas in (2), the design parameters are calculated for $Z_{0e} = 120.9$ Ω, $Z_{0o} = 20.7$ Ω, which is a -3-dB coupling coefficient and listed in Table 1. From Table 1, when $\Theta_{Ta} = 0°$ in Figure 1(b), the asymmetric equivalent circuit in Figure 1(b) is identical to the 90° directional coupler in Figure 1(a). With the gradual increase in Θ_{Ta}, the values of Z_{0ea} rise, while those of Z_{0oa} decrease, leading to the gradual increase in the coupling coefficients of $C_a = (Z_{0ea} - Z_{0oa})/(Z_{0ea} + Z_{0oa})$. The electrical lengths of Θ_a are inversely proportional to those of Θ_{Ta}. The coupling coefficient of C_a is equal to -3 dB in Figure 1(b) with $\Theta_{Ta} = 0°$ and features a gradual increase in Θ_{Ta}.

To show the differences between the original directional coupler in Figure 1(a) and its asymmetric equivalent circuit in terms of frequency responses, four cases with $\Theta_{Ta} = 0°$, 6°, 12°, and 18° in Table 1 were simulated, with the frequency responses plotted in Figure 3. The scattering parameters $|S_{41}|$ and $|S_{31}|$ of the asymmetric circuit are plotted in Figure 3(a), while the phase difference of $\angle S_{41} - \angle S_{31}$ is displayed in Figure 3(b). The two curves showing the frequency responses of $|S_{41}|$ and $|S_{31}|$ in Figure 3(a) meet at the design frequency of f_0 regardless of the choice of Θ_{Ta}. When $\Theta_{Ta} = 0°$, the two responses meet only once at f_0, but those with $\Theta_{Ta} \neq 0°$ intersect at two frequencies, one of which is f_0, while the other is greater than f_0. That is, the bandwidths of $|S_{41}|$ and $|S_{31}|$ increase with Θ_{Ta}. The phase responses

of $\angle S_{41} - \angle S_{31}$ are 90° in the frequency range of interest, as shown in Figure 3(b).

The symmetric equivalent circuit in Figure 1(c) consists of one CPL and four identical uncoupled TLs. The even- and odd-mode admittances of the CPL are $Y_{0es} = Z_{0es}^{-1}$ and $Y_{0os} = Z_{0os}^{-1}$, and the electrical length is Θ_s. The characteristic impedance and the electrical length of the uncoupled TLs are Z_T and Θ_{Ts}, respectively. Due to the symmetries, the design formulas can be derived easily [18].

Mixed Directional Coupler

The mixed equivalent circuit in Figure 1(d) consists of one CPL with the even- and odd-mode admittances of $Y_{0em} = Z_{0em}^{-1}$ and $Y_{0om} = Z_{0om}^{-1}$, electrical length of Θ_m, and four uncoupled TLs. The characteristic admittances of all four uncoupled TLs are the same, $Y_T = Z_T^{-1}$, and the two located diagonally are $\Theta_{Ts} + \Theta_{Ta}$ in length, while the two others are Θ_{Ts} long. The mixed topology in Figure 1(d) and Figure 4(a) may be changed to that in Figure 4(b), where the circuit in the dashed rectangle is a symmetric CPL topology, leading to the asymmetric equivalent circuit depicted in Figure 4(c).

The design formulas for Y_{0em}, Y_{0om}, and Θ_m can be derived by equating the circuit in the dashed rectangle in Figure 4(b) to the CPL with Z_{0ea}, Z_{0oa}, and Θ_a in Figure 4(c). Similar to the symmetric equivalent circuit, the relations in Figure 5 can be derived. The dashed rectangle in Figure 4(b) is again depicted in Figure 5(a), which is equivalent to the CPL with Y_{0ea}, Y_{0oa}, and Θ_a in Figure 5(b). Adding four identical TLs with Z_T and $-\Theta_{Ts}$ to all ports of both circuits in Figure 5(a) and (b) gives the two circuits in Figure 5(c) and (d). The topologies in Figure 5 are symmetric, and, therefore, even- and odd-mode excitation analyses may be applied, from which the design formulas can be obtained as

$$Y_{0em} = \sqrt{E_{em} E_{om}}, \tag{3a}$$

$$Y_{0om} = \sqrt{O_{em} O_{om}}, \tag{3b}$$

$$\tan\frac{\Theta}{2} = \sqrt{\frac{E_{em}}{E_{om}}} \text{ or } \sqrt{\frac{O_{em}}{O_{om}}}, \tag{3c}$$

where

$$E_{em} = Y_T \frac{Y_{0oa} \tan\dfrac{\Theta_a}{2} - Y_T \tan\Theta_{Ts}}{Y_T + Y_{0ea} \tan\dfrac{\Theta_a}{2} \tan\Theta_{Ts}},$$

$$E_{om} = Y_T \frac{Y_{0ea} \cot\dfrac{\Theta_a}{2} + Y_T \tan\Theta_{Ts}}{Y_T - Y_{0ea} \cot\dfrac{\Theta_a}{2} \tan\Theta_{Ts}},$$

$$O_{e\_m} = Y_T \frac{Y_{0oa} \tan\dfrac{\Theta_a}{2} - Y_T \tan\Theta_{Ts}}{Y_T + Y_{0oa} \tan\dfrac{\Theta_a}{2} \tan\Theta_{Ts}},$$

and

$$O_{om} = Y_T \frac{Y_{0oa} \cot\dfrac{\Theta_a}{2} + Y_T \tan\Theta_{Ts}}{Y_T - Y_{0oa} \cot\dfrac{\Theta_a}{2} \tan\Theta_{Ts}}.$$

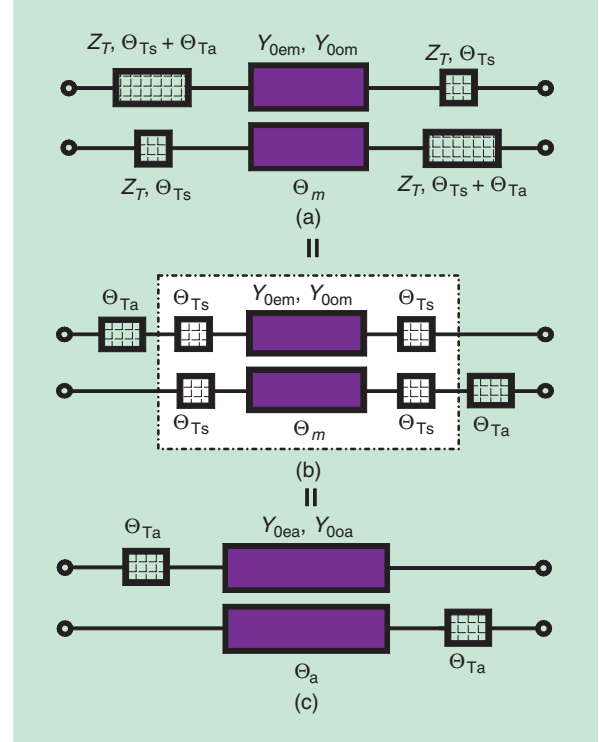Based on the formulas in (3), the design parameters for the mixed equivalent circuit in Figure 1(d)

Figure 4. *The mixed equivalent circuit. (a) The mixed equivalent circuit with four TLs. (b) The mixed equivalent circuit with six TLs. (c) The asymmetric equivalent circuit with Θ_{Ta}.*
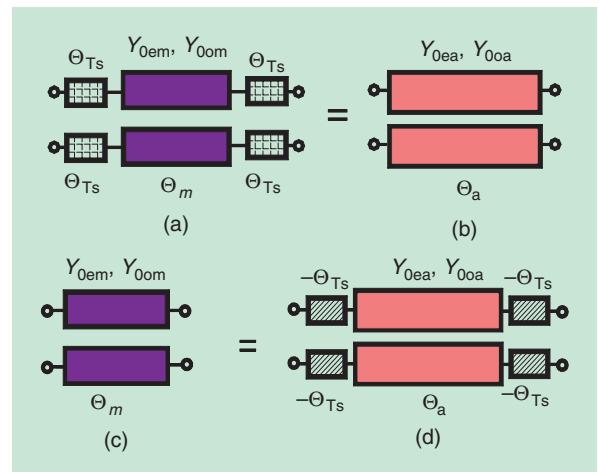

Figure 5. *The relations among mixed, asymmetric, and symmetric equivalent circuits. (a) The dashed-rectangle area in Figure 4(b) with Y_{0em}, Y_{0om}, and Θ_m. (b) A set of CPLs with Y_{0ea}, Y_{0oa}, and Θ_a. (c) A CPL with Y_{0em}, Y_{0om}, and Θ_m. (d) The symmetric equivalent circuit with Y_{0ea}, Y_{0oa}, and Θ_a.*

and Figure 4(a) were calculated for a proof-of-concept −3-dB directional coupler with a characteristic impedance of 50 Ω. The values of the even- and odd-mode impedances of Z_{0em} and Z_{0om} and the electrical lengths of Θ_m are listed in Table 2 for five different values of Θ_{Ts} and a fixed Θ_{Ta} of 5°. The frequency responses of the four cases in Table 2 are plotted in Figure 6. The results for $|S_{31}|$ and $|S_{41}|$ are shown in Figure 6(a), and the phase responses of $\angle S_{41} - \angle S_{31}$ are shown in Figure 6(b). The four mixed circuits are perfectly matched at f_0, and the bandwidths increase gradually with Θ_{Ts}. The phase differences of $\angle S_{41} - \angle S_{31}$ in Figure 6(b) show a constant 90°, regardless of the Θ_{Ts}.

TABLE 2. The design formulas for Z_{0em}, Z_{0om}, and Θ_m in a mixed equivalent circuit for $Z_{0e} = 120.9$ Ω and $Z_{0o} = 20.7$ Ω, fixing at $\Theta_{Ta} = 5°$.

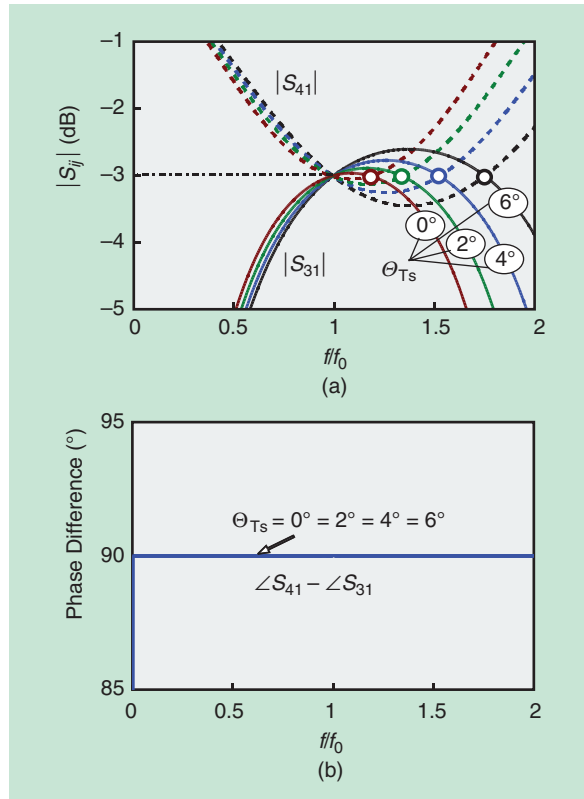| Θ_{Ts}	Z_{0em} (Ω)	Z_{0om} (Ω)	Θ_m (°)
0°	121.57	20.56	82.91
2°	123.1	20.31	77.2
4°	125.64	19.9	71.43
6°	129.43	19.32	65.55
8°	134.86	18.54	59.51

Figure 6. *The frequency responses of a mixed directional coupler with $\Theta_{Ta} = 5°$ fixed. (a) $|S_{31}|$ and $|S_{41}|$. (b) The phase difference of $\angle S_{41} - \angle S_{31}$.*

Application of Asymmetric Equivalent Circuits to Marchand Baluns

The asymmetric, symmetric, and mixed equivalent circuits in Figure 1(b)–(d) can be substituted for two 90° CPLs of the Marchand baluns [38] with connecting segments. The asymmetric circuits are investigated first for arbitrary termination-impedance values as a proof-of-concept demonstration. By changing the locations of the uncoupled TLs of each asymmetric equivalent circuit, three cases of the connecting segments are possible, one of which is depicted in Figure 7(a), while its isolation circuit is in Figure 7(b). The termination impedance at port 1 is R_r; at ports 2 and 3, it is R_L, as shown in Figure 7(a). The isolation circuit uses two 90° identical TLs with characteristic impedance Z_i and isolation resistance R_i. The asymmetric circuit connected at port 1 is AC1, and the one connected at port 3 is AC2. The even-/odd-mode admittances and electrical length of AC1 are Y_{0ea1}, Y_{0ea1}, and Θ_{a1}, while those of AC2 are Y_{0ea2}, Y_{0ea2}, and Θ_{a2}. The electrical lengths of the uncoupled TLs of AC1 and AC2 are Θ_{Ta1} and Θ_{Ta2}, respectively, and the characteristic impedance of both uncoupled TLs are equally the same as Z_T. The connecting segment can be assumed to be the superposition of the two TLs, with a total length of $\Theta_{Ta1} + \Theta_{Ta2}$, thus enabling its accurate simulation and modeling.

As a proof-of-concept demonstration of the proposed equivalent circuits to realize complicated structures using the asymmetric circuits with arbitrary coupling coefficients and terminating impedances, an impedance-transforming (100 into 50 Ω) Marchand balun was designed at 2 GHz and fabricated. When
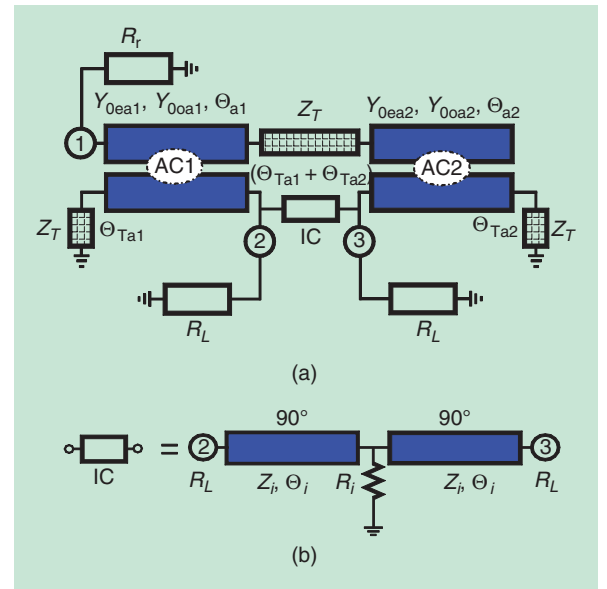

Figure 7. *The impedance-transforming Marchand balun with the connecting segment. (a) The Marchand balun. (b) The isolation circuit. IC: isolation circuit.*

$R_r = 100\ \Omega$, $R_L = 50\ \Omega$ and $C = -6$ dB for the directional coupler of the Marchand balun, while $Z_{0e} = 100.48\ \Omega$ and $Z_{0o} = 33.39\ \Omega$, using [38, eq. (9)]. Assuming a connecting segment of 30°, the values of $\Theta_{Ta1} = \Theta_{Ta2} = 15°$ were chosen, thus leading to $Z_{0ea1} = Z_{0ea2} = 102.91\ \Omega$, $Z_{0oa1} = Z_{0oa2} = 32.60\ \Omega$, and $\Theta_{a1} = \Theta_{a2} = 72.6°$, using (2), resulting in $Z_T = 57.92\ \Omega$. The isolation circuit is dependent on the termination impedances of R_L, and, if the isolation resistance of R_i is chosen to be an available resistance of 86.6 Ω, the characteristic impedance of Z_i is computed as 93.06 Ω, referring to [38, eq. (11)]. The fabricated circuit is illustrated in Figure 8, where the connecting segment is indicated.

For further applications of the CPLs, two-port CPLs need to be discussed. The respective two-port CPLs can be obtained by terminating two ports of the directional coupler in Figure 1(a) in a diagonal configuration (in this example, ports 3 and 4) in open/short circuits called, respectively, *two open circuits in a diagonal direction* (*TO*) and *two short circuits in a diagonal direction* (*TS*). TOs and TSs have been employed for diverse applications that are investigated in later sections.

TOs

The TO topology and its equivalent circuit are shown in Figure 9(a) and (b), respectively. The equivalent circuit at a design frequency of $f_0 = \omega_0/(2\pi)$ consists of one TL with the characteristic impedance of Z_T, electrical length of Θ, and two identical series capacitances of C_o, where $Z_T = (Z_{0e} - Z_{0o})/2$ and $\omega C_o = Z_{0o}^{-1}\tan\Theta = Y_{0o}\tan\Theta$.

Using (1), several 90° TOs with $Z_0 = 50\ \Omega$ were designed by varying the coupling-coefficient values (−3, −5, −7, and −10 dB); their frequency responses are plotted in Figure 10. The frequency responses show that the TO is nearly perfectly matched only for $C = -3$ dB, while the matching for the other cases gradually deteriorates for smaller C values. To ensure near-perfect matching regardless of the coupling coefficient, the design formulas in (1) should be modified as discussed in the next section.

DC Blocks

One application for the TO is a dc block [33]. Such blocks are passive components that prevent dc current flow while allowing RF power through. They can feature two different frequency responses: Chebyshev (equal ripple) and Butterworth (maximally flat), as plotted in Figure 11 [33], [34] showing the variation of $|S_{21}|^2$ as a function of the frequency $\Omega = \cot\Theta$ for $\Theta = 90°$ at a design frequency of f_0. To realize the Chebyshev response in Figure 11(a), $f(0) = f(\Omega_c) = 1 - R_{ip}^2$, and $f(\Omega_m) = 1$, where R_{ip}^2 is the maximum allowable ripple value at $\Theta = 90°$ that can be correlated to the insertion loss, IL, and return loss, RL, through the following equations:

$$R_{ip}(\text{dB}) = \sqrt{1 - 10^{\frac{-IL(\text{dB})}{10}}}, \tag{4a}$$

$$R_{ip}(\text{dB}) = 10^{\frac{-RL(\text{dB})}{20}}. \tag{4b}$$

The bandwidth of the Chebyshev response is defined as $2\ \Omega_c$, as shown in Figure 11(a). For the Butterworth response in Figure 11(b), $f(0) = 1$ should be satisfied. The main difference between the two response types is the frequency value at which the maximum $|S_{21}|^2$ exists. In both cases, the coupling coefficient is defined as
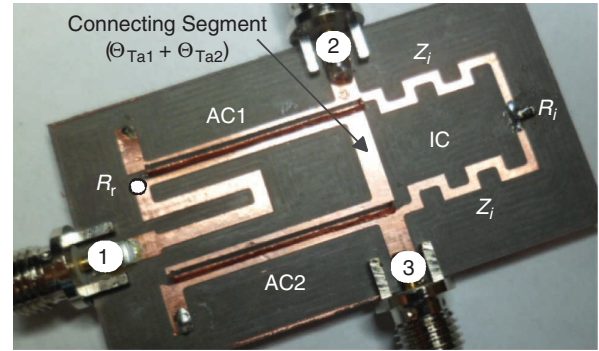
$$C = \frac{Z_{0e} - Z_{0o}}{Z_{0e} + Z_{0o}}. \tag{5}$$

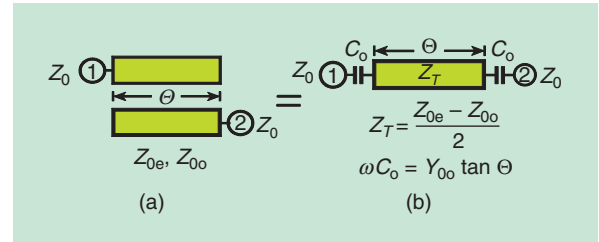**Figure 8.** *The fabricated Marchand balun with the connecting segment [18].*

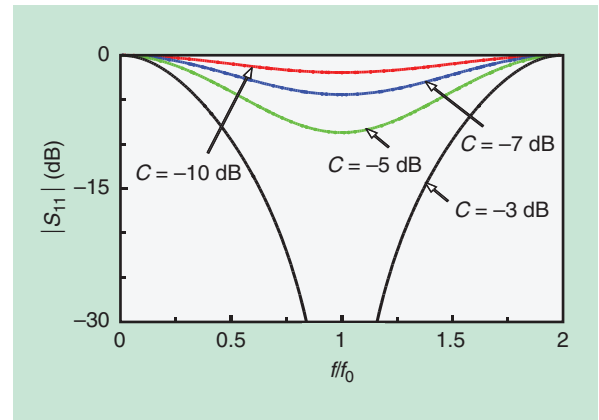**Figure 9.** *The TO. (a) The topology and (b) equivalent circuit.*

Figure 10. *The frequency responses of the TOs for different coupling coefficients with the conventional design formulas, such as (1).*
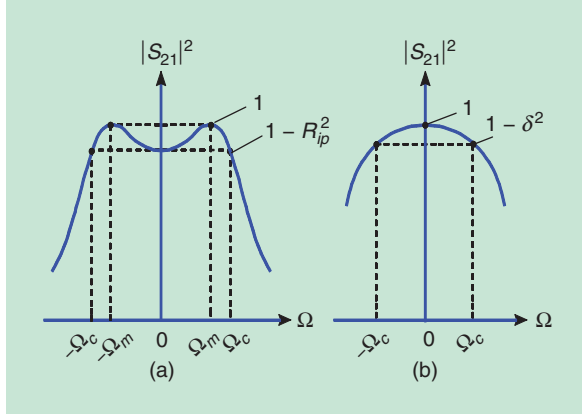
Figure 11. *The frequency responses of dc blocks (TOs). (a) The Chebyshev (equal ripple) response. (b) The Butterworth (maximally flat) response.*

TABLE 3. The bandwidths of the dc blocks for Chebyshev responses, with $Z_0 = 50\ \Omega$ and $RL = 15$ dB at f_0.

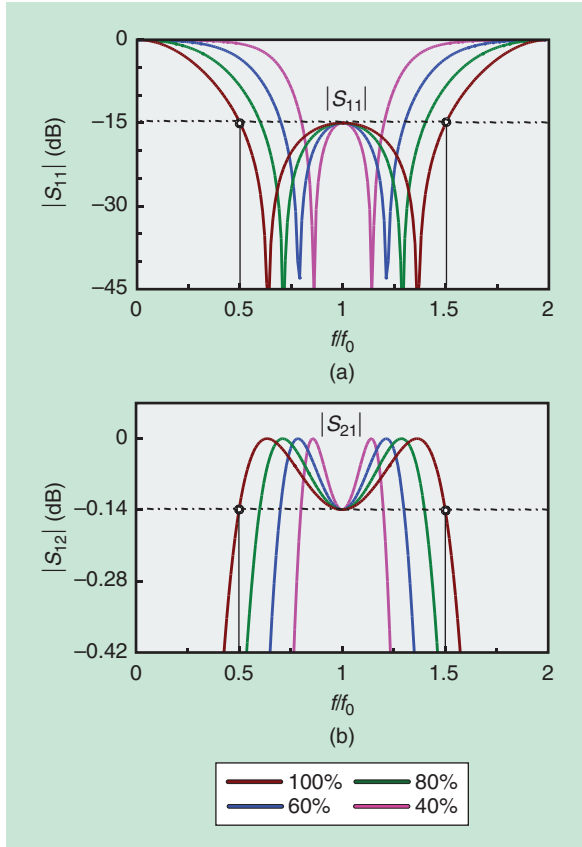| Bandwidth (%)	100%	80%	60%	40%
C (dB)	−2.38	−3.58	−5.408	−8.37
$Z_{0e}\ (\Omega)$	138.54	150.19	171.3	216.68
$Z_{0o}\ (\Omega)$	18.85	30.5	51.61	96.99

Figure 12. *The Chebyshev responses for a maximum return loss of 15 dB for various design bandwidths. (a) $|S_{11}|$ and (b) $|S_{21}|$.*

To achieve the Butterworth response in Figure 11(b), combining $f(0) = 1$ and the coupling-coefficient expression (5), the design formulas [33, eq. (24)] are derived as

$$Z_{0e} = Z_0 \frac{1+C}{C}, \tag{6a}$$

$$Z_{0o} = Z_0 \frac{1-C}{C}. \tag{6b}$$

To realize the Chebyshev response in Figure 11(a), combining $f(0) = 1 - R_{ip}^2$ and the coefficient expression (5), the design formulas [33, eq. (14)] are derived as

$$Z_{0e} = Z_0 \sqrt{\frac{1+R_{ip}}{1-R_{ip}}} \frac{1+C}{C}, \tag{7a}$$

$$Z_{0o} = Z_0 \sqrt{\frac{1+R_{ip}}{1-R_{ip}}} \frac{1-C}{C}. \tag{7b}$$

The following important design formula from [33, eq. (18)] for the bandwidths can be directly derived from the condition of $f(\Omega_c) = 1 - R_{ip}^2$, such as

$$\Omega_c^2 = \cot^2 \Theta_c = \frac{4C^2 R_{ip}(1 + R_{ip} - C^2)}{(1 + R_{ip})^2 (1 - C^2)^2}, \tag{8}$$

where the bandwidth, BW, can be derived from Θ_c, as in [33, eq. (21)], through the following equation:

$$\Omega_c = \cot\left\{ \frac{\pi}{2}\left(1 - \frac{BW}{2}\right) \right\}, \tag{9}$$

where $f_1 = f_0 \Theta_c / 90$ and $f_2 = f_0(2 - \Theta_c / 90)$, with the unit of Θ_c in degrees, leading to BW $= 2(f_2 - f_1)/(f_2 + f_1)$.

For the design of dc blocks with specific Chebyshev responses, the maximum allowable ripple value, R_{ip}, must be determined from the *IL* and *RL* specifications through (4). Based on the design bandwidth, the value of Θ_c, must be calculated through (8). For these calculated values of R_{ip} and Θ_c, the realized coupling coefficient C values can be calculated across the desired bandwidth in (9). For example, if a maximum return loss of $RL = 15$ dB is desired across the bandwidth of operation, R_{ip} is calculated as 0.1778 by (4b). Table 3 lists the realized coupling coefficients for this value of R_{ip} and different bandwidth specifications, verifying that higher coupling coefficients can be realized for wider bandwidths. Based on the design parameters in Table 3, the four proof-of-concept dc-block prototypes were simulated with the Advanced Design System (ADS) circuit simulator, and the frequency responses plotted in Figure 12 confirmed the theoretical calculations.

For the Butterworth responses, the even- and odd-mode impedances were calculated using (6) by varying the coupling-coefficient values between −3 dB and

−10 dB; the frequency responses are plotted in Figure 13. Compared to the frequency responses for similar structures using the conventional design formulas in Figure 10, all of the TO-based dc blocks are perfectly matched at 1 GHz, with bandwidths that are directly proportional to the coupling-coefficient values.

Impedance-Transforming Wideband Compact dc Blocks

For the 90° dc blocks, approximate design formulas were developed for the symmetric and asymmetric structures in 1980 [35] and 1986 [36], respectively. The improved design formulas were derived for the symmetric and asymmetric dc blocks in [33] and [34]. If the effective electrical lengths of the dc blocks are 90° at the design frequency [33]–[36], real impedance transforming for diverse applications is possible. Because wireless communication systems require a low weight and small footprint, the compact dc blocks are of interest. Several compact dc blocks have been reported in the literature [22]–[26]. However, the bandwidths are all small (lower than 40%) [22]–[26], and the sizes are not compact. To overcome the conventional problems with small bandwidths, impedance-transforming wideband and compact 90° dc blocks (WCDCs) are investigated.

The 90° dc block and its WCDC [20] are depicted in Figure 14(a) and (b), respectively, where the even- and odd-mode impedances of the 90° dc block are Z_{0eR} and Z_{0oR}. The WCDC consists of a CPL with even- and odd-mode impedances of Z_{0ec} and Z_{0oc} and electrical length of Θ_c. Two ports of the CPL are terminated in two identical susceptances, (jS_c), and they can have wide bandwidths and are compact because the CPL is designed by the pole-split (PS) (root) method [33], [34], [47] and the transmission-zero movement (TZM) method.

PS Method

In a filter design, the number of stages (orders) needs to grow to increase the bandwidth. However, with no rise in the number of stages, the bandwidth can be widened by the PS method, which is not a conventional filter-design technique because the structure itself is not changed, while the responses are altered to have wider bandwidths by the design formulas. One example is the dc blocks with Chebyshev responses shown in Figure 12 [33], [34]; another is the Butter-Cheby filters [47].

TZM Method

The TZM method has been used for diverse applications to increase bandwidth. For example, consider three dc blocks conceived for a design frequency of 1 GHz and that are 90, 60, and 40° long at 1 GHz. The

even- odd-mode impedances are 103.4 Ω and 23.4 Ω for both termination impedances of 40 Ω. The dc blocks' frequency responses are plotted in Figure 15, where the 90° dc block is perfectly matched at 1 GHz. The two others are not matched at 1 GHz and perfectly matched at 1.52 and 2.26 GHz, respectively. The bandwidths that can cover the 15-dB return loss in Figure 15 are indicated by red, black, and blue lines with $\Delta_{40°}$, $\Delta_{60°}$, and $\Delta_{90°}$, respectively; the red line, with $\Delta_{40°}$, is the longest. The bandwidths with the 15-dB return loss are inversely proportional to the electrical lengths of the dc blocks. The reason is that the first TZ frequencies of
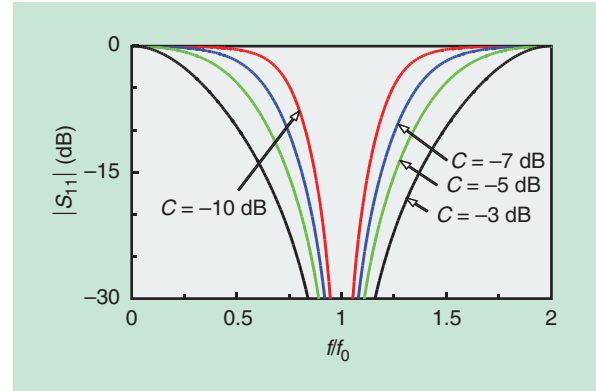

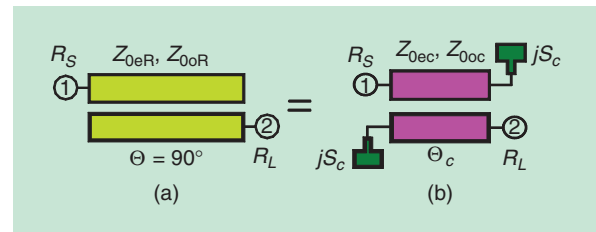**Figure 13.** The Butterworth responses of TO-based dc blocks for different values of the coupling coefficient.

Figure 14. (a) The impedance-transforming 90° dc block (90° TO) and (b) the WCDC [20].
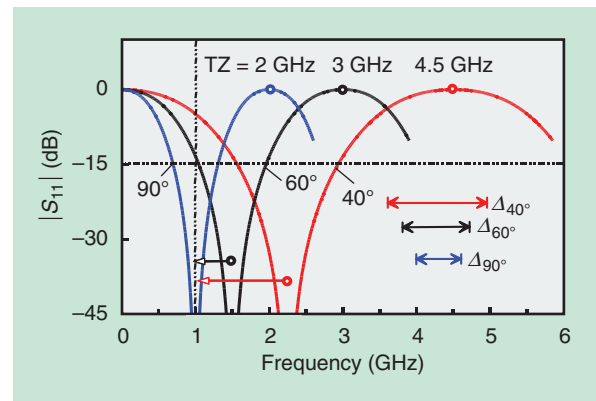

Figure 15. The frequency responses of $|S_{11}|$ of dc blocks with electrical lengths of 90, 60, and 40° at 1 GHz.

the 90, 60, and 40° dc blocks (except 0 GHz) are moved to a higher frequency region, such as 2, 3, and 4.5 GHz, as shown in Figure 15. By fixing the TZ frequencies, the matching frequency of the 60° or 40° dc block must be shifted to the design frequency of 1 GHz to make the coverage form from approximately 1 GHz. Moving the matching frequency requires building a matching circuit using a 60° or 40° dc block by adding susceptances so that the resulting circuits can be perfectly matched at 1 GHz and the effective electrical lengths are 90° at 1 GHz. For this, careful matching processes are required.

The design formulas for the WCDCs are given as

$$\cos\Theta_c = \frac{\cos\Theta_T\{4S_c^2 + \tan^2\Theta_T(Y_{0eR} - Y_{0oR})^2\}}{2S_c(Y_{0eR} + Y_{0oR})}, \quad (10a)$$

$$Y_{0ec} = Z_{0ec}^{-1} = \frac{2S_c^2\csc\Theta_T}{\csc\Theta_c}\psi_e, \quad (10b)$$

$$Y_{0oc} = Z_{0oc}^{-1} = \frac{2S_c^2\csc\Theta_T}{\csc\Theta_c}\psi_o, \quad (10c)$$

where $\Theta_T \neq 0$, $S_c = \sqrt{Y_{0eR}Y_{0oR}}\tan\Theta_T$, $Y_T = \sqrt{Y_{0eR}Y_{0oR}}$, (10d)

$$\psi_e = \frac{(\cot\Theta_T + \csc\Theta_T)Y_{0eR} + (\cot\Theta_T - \csc\Theta_T)Y_{0oR}}{(2S_c\cot\Theta_T)^2 - \tan^2\Theta_T(Y_{0eR} - Y_{0oR})^2}, \quad (10e)$$

$$\psi_o = \frac{(\cot\Theta_T - \csc\Theta_T)Y_{0eR} + (\cot\Theta_T + \csc\Theta_T)Y_{0oR}}{(2S_c\cot\Theta_T)^2 - \tan^2\Theta_T(Y_{0eR} - Y_{0oR})^2}. \quad (10f)$$

For the 90° dc block in Figure 14(a), $Z_{0eR} = 103.4\ \Omega$ and $Z_{0oR} = 23.4\ \Omega$ can be calculated for $C = -4$ dB and $R_s = R_L = Z_0 = 40\ \Omega$. When the value of S_c^{-1} is given as 278.9 Ω in Figure 14(b), substituting the values of S_c^{-1}, $Z_{0eR} = 103.4\ \Omega$, and $Z_{0oR} = 23.4\ \Omega$ into (10) gives the even- and odd-mode impedances of $Z_{0ec} = 105.1\ \Omega$ and $Z_{0oc} = 23.02\ \Omega$ and the electrical length of $\Theta_c = 77.07°$ for the WCDCs. In this way, the design parameters in Table 4 can be obtained, where $Z_T = 49.18\ \Omega$ can be calculated from $Z_T = \sqrt{Z_{0eR}Z_{0oR}}$ and the values in parentheses are for Θ_T to have the required values of S_c^{-1}.

With the electrical length of Θ_c reduced from 90°, the values of Z_{0ec} increase, and those of Z_{0oc} decrease to make up for the lack of coupling generated by the shorter coupling lengths. Based on the design parameters in Table 4, the WCDCs were simulated with ADS; the frequency responses of $|S_{11}|$ are plotted in the range

TABLE 4. The design parameters for Z_{0ec}, Z_{0oc}, and Θ_c for $Z_{0eR} = 103.40\ \Omega$ and $Z_{0oR} = 23.40\ \Omega$.

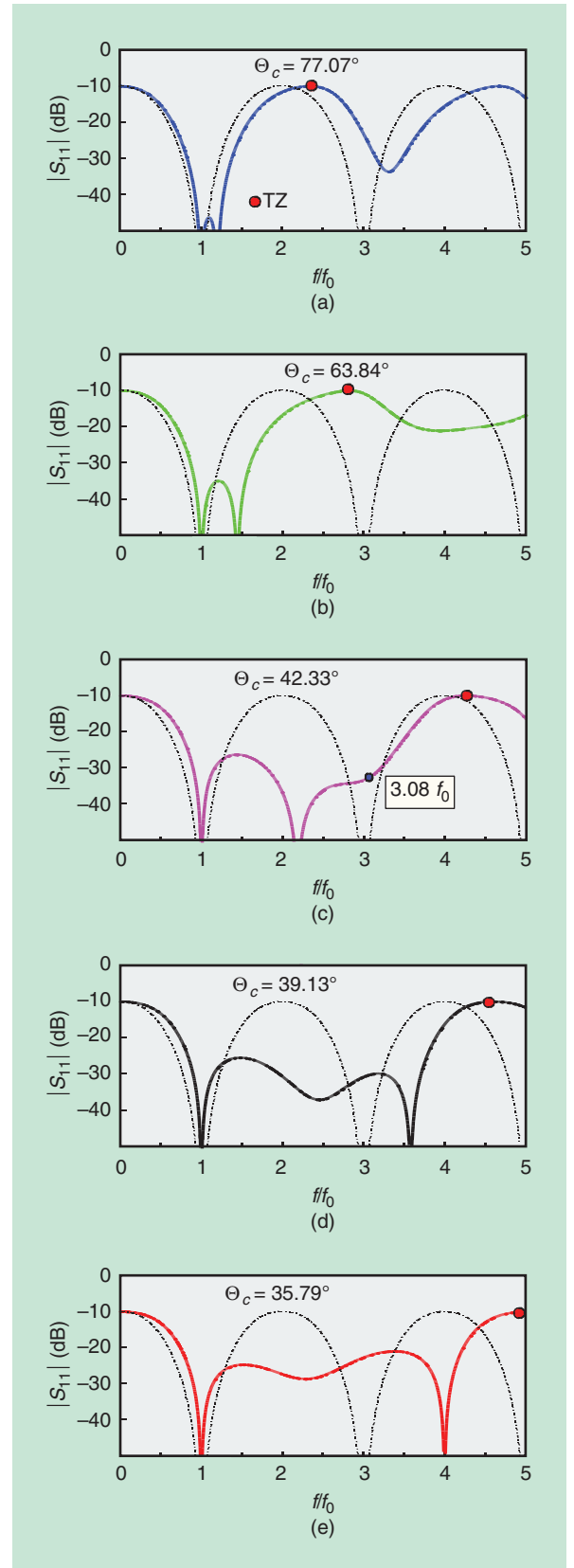| $S_c^{-1}(\Omega)$	Z_{0ec} (Ω)	Z_{0oc} (Ω)	Θ_c (°)
278.93 (10°)	105.1	23.02	77.07
135.13 (20°)	110.93	21.81	63.84
70.24 (35°)	136.53	17.72	42.33
65.27 (37°)	143.61	16.84	39.13
60.74 (39°)	152.64	15.85	35.79

Figure 16. *The frequency responses of $|S_{11}|$ with $C = -4$ dB. (a) $\Theta_c = 77.07°$. (b) $\Theta_c = 63.84°$. (c) $\Theta_c = 42.33°$. (d) $\Theta_c = 39.13°$. (e) $\Theta_c = 35.79°$.*

of (0–5) f_0 in Figure 16, where the dotted lines show the original 90° dc block with the Butterworth response and solid lines indicate the WCDCs in Figure 14(b). Each susceptance, S_c, was realized with an open stub that had the uniform characteristic impedance of 49.18 Ω from (10d).

The maximum number of roots for the solutions to $S_{11}(f/f_0) = 0$ in [20, eq. (11)] is four in a range of 0–(180°/Θ_c)f_0, and the real roots are called *poles*. All of the WCDCs in Figure 16 are perfectly matched at f_0, and the bandwidth with the return loss of $L_R = 10$ dB of the 90° dc block is roughly 0.6–1.41 f_0 (81%). The 10-dB bandwidth with $\Theta_c = 77.07°$ in Figure 16(a) is 0.65–1.585 f_0 (93.5%), while the 10-dB bandwidth for $\Theta_c = 64.84°$ in Figure 16(b) is 0.69–1.86 f_0 (117%). The WCDCs with $\Theta_c = 42.33, 39.13,$ and 35.79° in Figure 16(c)–(e) are 0.74–3.57 f_0 (283%), 0.74–3.9 f_0 (316%), and 0.74–4.24 f_0 (350%), respectively, and inversely proportional to the electrical length of Θ_c.

When $\Theta_c = 90°$, the WCDC becomes the original 90° dc block, and the two poles for the perfect matching overlap at f_0. When Θ_c becomes shorter than 90°, any value of S_c is needed for perfect matching at f_0, as explained in Figure 15, and the two overlapped poles at f_0 start to be split (PS method). For $\Theta_c = 77.07°$ in Figure 16(a), one pole is at f_0, and another is at 1.2 f_0. For $\Theta_c = 42.33°$ in Figure 16(c), two poles exist at f_0 and 2.18 f_0, and two complex roots exist at roughly 3.08 f_0 and can be developed into real roots with slight changes. As the electrical lengths of Θ_c become shorter, the two roots (poles) close to the transmission zeros [0 GHz and (180°/Θ_a)f_0] are located farther away, which is the main reason for the wider bandwidths. The TZs are moved farther, as the red dots in Figure 16 indicate, which is the definition of the TZM method.

For the measurements, the electrical length of Θ_c in Table 4 is chosen as 39.13°, where the corresponding values are $Z_{0ec} = 143.61$ Ω, $Z_{0oc} = 16.84$ Ω, and $S_c^{-1} = 65.27$ Ω. To realize S_c, two TLs connected in a cascade are employed, one of which is a high-impedance line and the other a low-impedance one. The characteristic impedances of the high-/low-impedance lines are 140 and 35 Ω, and the electrical lengths are 6 and 22° at 1 GHz, with the form in [31, Fig. 13(b)]. One side of the low-impedance line is open-circuited, and the other side is connected to the high-impedance line, which is located between the low-impedance line and the CPL. Since the CPL requires a tight coupling (greater than –3 dB), a 2D microstrip format may be impossible, so the 3D vertically installed planar structure in [18, Fig. 18(b)] was applied for the fabrication.

Even though the WCDC is terminated in 40 Ω, a 50-measurement system may be used without impedance transformers, since the impedance, admittance,

and *ABCD* parameters of the WCDC are not changed by the termination impedances; only the scattering parameters are altered. Using that idea, the WCDC is measured with 50-Ω feeding lines that have the assumed electrical length of Θ_f, as shown in Figure 17(a). After measuring the scattering parameter of the WCDC with 50-Ω termination impedances, the measured data are saved in the ADS data item, as shown in Figure 17(b). To remove the feeding-line effect, a 50-Ω feeding line is connected but with $-\Theta_f$. If the circuit in the ADS data item in Figure 17(b) is simulated after terminating the wanted impedances of 40 Ω at both ports, the desired measured data can be obtained.

A fabricated WCDC is displayed in Figure 18(a), and the measured frequency responses of $|S_{11}|$ and $|S_{12}|$ are in Figure 18(b), with an expanded view of $|S_{12}|$ in Figure 18(c). The measured bandwidth with a 10-dB return loss in Figure 18(b) spans the range of 0.74–4.05 GHz (331%) with a design frequency of 1 GHz, featuring ultrawideband performance even though it is very compact. At the design frequency of 1 GHz, the measured $|S_{12}|$ is approximately –0.634 dB.

TSs

Figure 19 depicts a typical TS topology as well as its equivalent circuit [48] consisting of one TL with characteristic admittance of $Y_T = (Y_{0o} - Y_{0e})/2$, electrical length of $\pi + \Theta$, and two identical shunt inductances of L_0, where $\omega L_0 = Z_{0e} \tan \Theta$. The peculiar feature of the TS is the introduction of an additional phase of 180° by short-circuiting two ports in a diagonal configuration, thus making it a good candidate for numerous applications, such as compact coupled-line ring hybrids (CRHs) [19], [28]–[32]. Another special feature of this topology, discussed in the section "High-Impedance TL Sections," is its easy realization of very high values of the characteristic impedance of $Z_T = Y_T^{-1}$, which can be used in the realization of high-impedance TLs and power dividers (ring
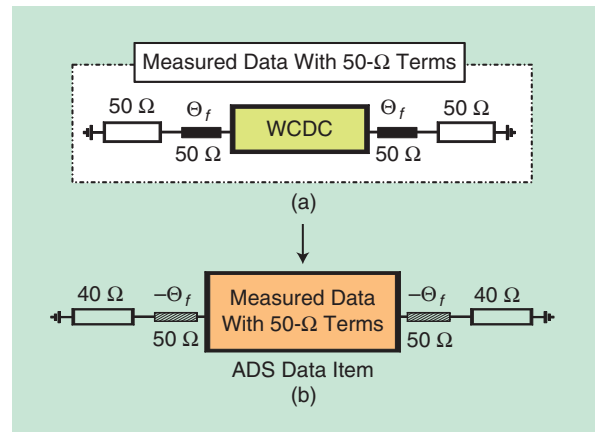

Figure 17. *The measured data transformation. (a) The 50-Ω and (b) 40-Ω termination impedances.*

and branch-line hybrids and Wilkinson power dividers) with high power-division ratios [18], [32], [43], [44].

Compact CRHs

The conventional ring-hybrid configuration, as shown in Figure 20(a), consists of three 90° and one 270° TLs having the characteristic impedances of Z_1, Z_2, Z_3, and Z_4 [31]. In the case that all four ports are terminated in
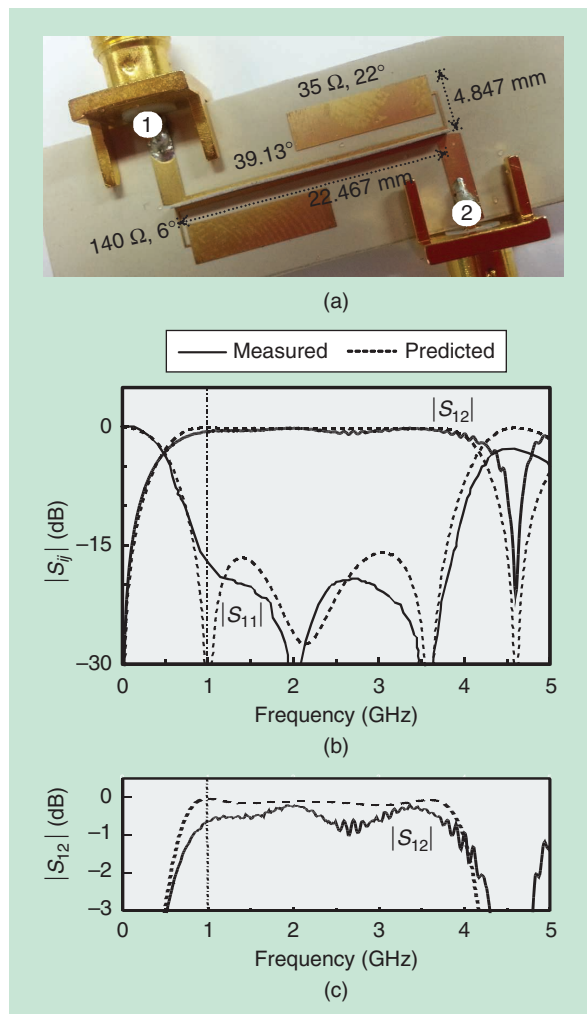

Figure 18. *(a) The fabricated WCDC [20]. (b) The measured and predicted frequency responses of $|S_{12}|$ and $|S_{11}|$. (c) The closed view of $|S_{12}|$.*
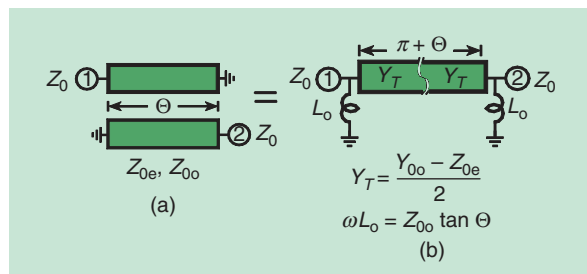

Figure 19. *The TS (a) topology and (b) equivalent circuit.*

the same impedance, Z_0, the characteristic impedances should satisfy the relationship of $Z_1 = Z_3$ and $Z_2 = Z_4$, and, for equal power-division ratios, or 3-dB ring hybrids, the characteristic impedance of all four sections should be the same: $Z_1 = Z_2 = Z_3 = Z_4 = \sqrt{2}\,Z_0$. If the operating frequencies are below 5 GHz, the hybrid's area is relatively large, especially for microstrip implementations, and numerous publications have aimed to miniaturize it. One of the most common solutions to reduce the electrical length is to replace the 270° TL with a 90° TS, as displayed in Figure 20(b). Perfect matching can be achieved only if the coupling coefficient is –3 dB, similar to the effect observed for TOs. To guarantee perfect matching regardless of the coupling coefficient, the design formulas should be modified as

$$Z_{0e} = Z_0 \frac{C}{1-C}, \; Z_{0o} = Z_0 \frac{C}{1+C}, \tag{11}$$

where the design formulas in (11) result in a maximally flat (Butterworth) response. These hybrid topologies are known as CRHs [19], [28]–[32] because of the TSs used in the miniaturized ring hybrids, as presented in Figure 20(b).

To achieve a further size reduction, the three equivalent circuits of the TLs in Figure 21 [31] can be used. The one in Figure 21(a) is called the *stepped-impedance, coupled-line Π-type (SCΠ)*. The other two topologies in Figure 21(b) and (c) are known as the *stepped-impedance modified T-type (SMT)* and *stepped-impedance modified Π-type (SMΠ)*, respectively. Both the SMT and SMΠ are the equivalent circuits for the 90° TLs, while the SCΠ is for the 270° TL and 90° TS. The SCΠ in Figure 21(a) consists of a TS and two identical open stubs and TLs. The even- and odd-mode impedances of the TS are Z_{0e} and Z_{0o}, with electrical length Θ_{sC}. The characteristic impedances of the "feeding" TLs and open stubs are Z_a and Z_{oC}, with electrical lengths of Θ_a and Θ_{oC}, respectively. Through the addition of the feeding TLs with Z_a and Θ_a in Figure 21(a), it is easier to connect the TS to other TLs and ports because the points where two open stubs are
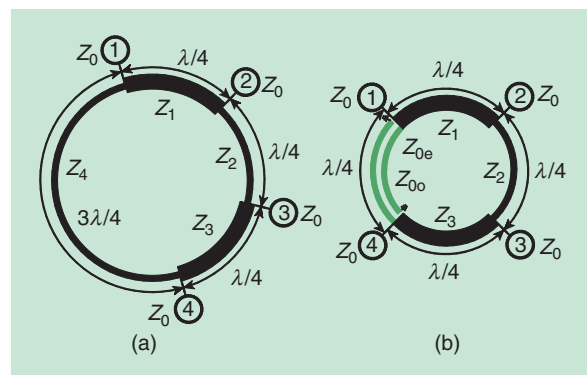

Figure 20. *The (a) conventional and (b) CRH topologies [28]–[32].*

connected to the TS do not need to be placed in a straight line. The SMT shown in Figure 21(b) is composed of two identical TLs with Z_a and Θ_a and a modified T-equivalent circuit (MT) [38], while the SMΠ shown in Figure 21(c) also includes two identical TLs with Z_a and Θ_a and a modified Π-equivalent circuit [38].

Without loss of generality and as a proof-of-concept demonstration, letting $\Theta_a = 0°$ and fixing $N\Theta_{sT} = N\Theta_{sΠ} = 50°$ for the SMT and SMΠ topologies in Figure 21(b) and (c), the S_{22} parameter values at the 100-Ω terminated port of the impedance transformers converting 50 into 100 Ω were simulated by varying the number of stages, N. The simulation results are shown on a Smith chart normalized to 100 Ω (see Figure 22) for the operating frequencies between 0 and 2 GHz and the design frequency of 1 GHz. The quarterwave impedance transformer expressed as "90° TL" in Figure 22 forms a circle (reference) intersecting the two points of 50 Ω (normalized value: 0.5) and 100 Ω (normalized value: 1). The SMΠ with $N = 3$ forms a circle that is very similar to that of the 90° TL. The SMΠ with $N = 2$ also forms a circle but slightly deviates from the reference circle with the 90° TL. However, the trajectories of the SMΠ with $N = 1$ and SMT with $N = 1$ don't form a circle and diverge from the reference.

From the results of the scattering parameters of S_{22}, it can be concluded that the number of N should be greater than or equal to three for performance similar to that of conventional (typically longer) matching structures. For an N greater than three, the bandwidths of the SMΠs and SMTs are roughly the same as that of the 90° TL, even though their physical sizes are much smaller than the one corresponding to the 90° quarterwavelength transformer, which is a unique feature of the proposed miniaturization approach, since the achieved bandwidths of the conventional passive components are proportional to the physical size.

Using the equivalent circuits in Figure 21, compact CRHs can be easily fabricated, and two proof-of-concept 3-dB coupled-line prototypes are presented in Figure 23. The bandwidths of the two cases are 26 and 57%, respectively, and are larger than that of the conventional one that has approximately 10% bandwidth, even though their total TL lengths are much smaller than the conventional type (540° long). This confirms that the deployment of the TSs and their equivalent circuits in Figure 21 enables not only miniaturization but also significantly wider bandwidths.

High-Impedance TL Sections

As the operating frequencies and complexity level of RF modules become increasingly higher, the substrates of planar TLs, such as coplanar waveguides and microstrips, become thinner while featuring higher dielectric-constant values, especially for flexible and conformal RF structures. In this case, high characteristic-impedance values greater than 140 Ω are not easy to fabricate in microstrip technologies. The use of TSs can alleviate this issue.

In the equivalent circuit of the TS in Figure 19(b), the characteristic impedance of $Z_T = Y_T^{-1}$ can be expressed as

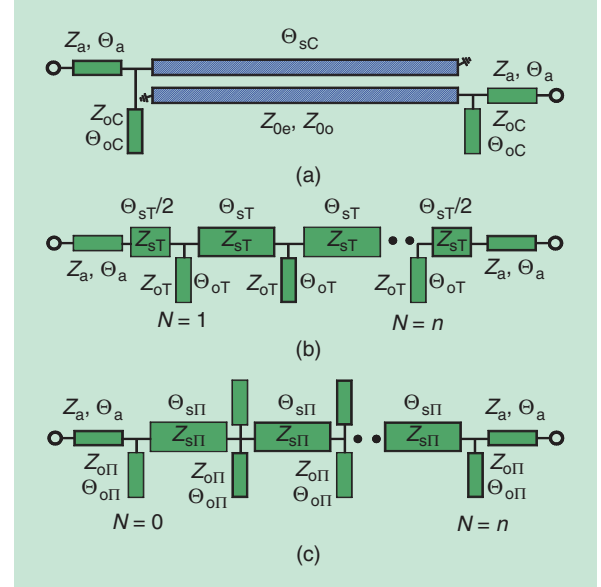$$Z_T = \frac{2Z_{0e}}{\frac{Z_{0e}}{Z_{0o}} - 1}. \tag{12}$$

Figure 21. *The 270° and 90° TL equivalent circuits for the characteristic impedance of Z_0 [31]. (a) The SCΠ for a 270° TL. (b) The SMT for a 90° TL. (c) The SMΠ for a 90° TL.*
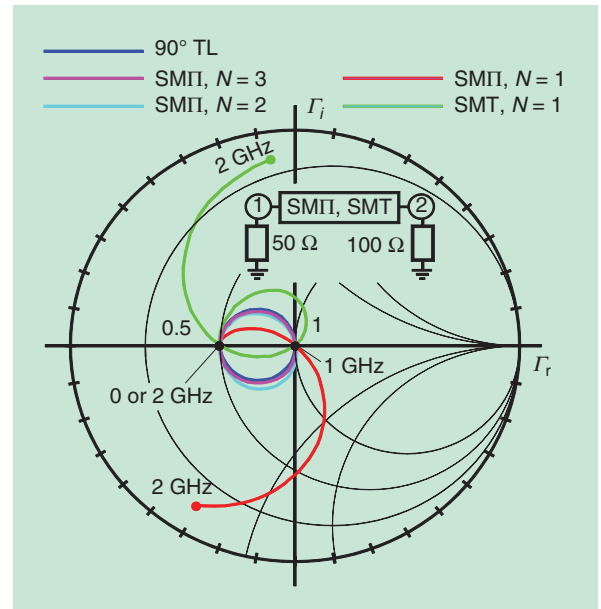

Figure 22. *The scattering-parameter values of S_{22} on an impedance Smith chart normalized to 100 Ω [31].*
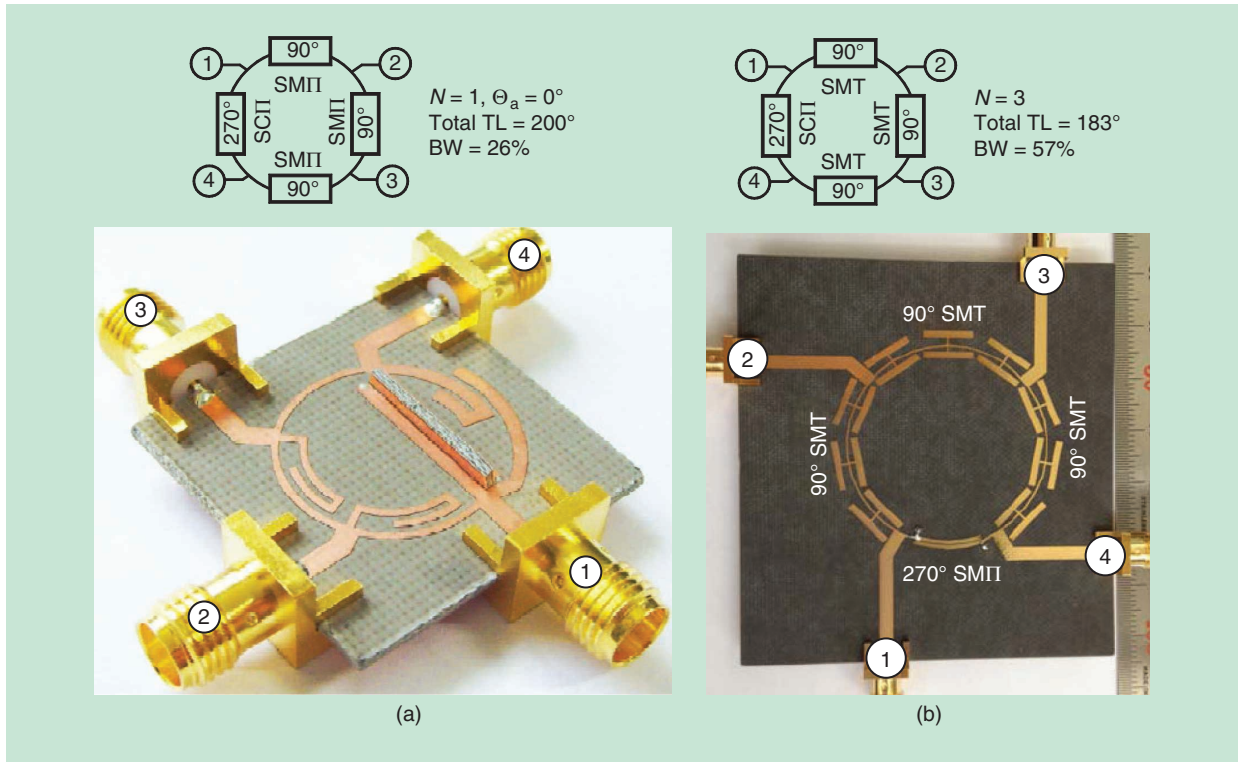
Figure 23. *The fabricated 3-dB CRHs [30], [31]. (a) The combination of the SCΠ (Θ_a = 0°) and SMΠ (N = 1, and Θ_a = 0°) sections [30]. (b) The combination of the SMT (N = 3, and Θ_a = 0°) and SCΠ (Θ_a ≠ 0°) sections [31].*
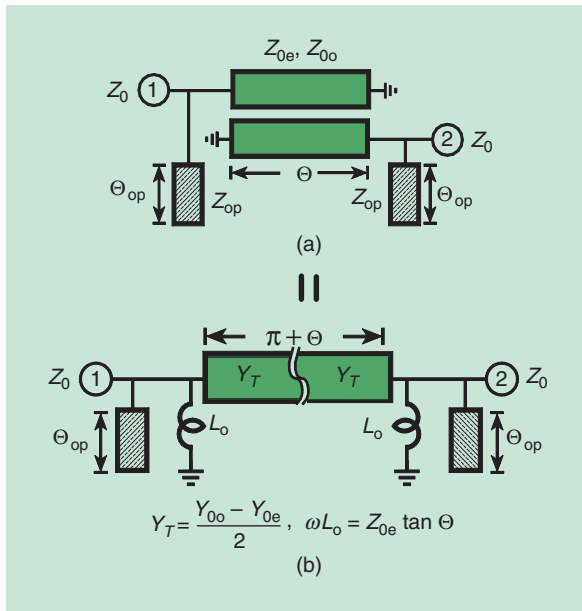

Figure 24. *The high-impedance TL implementation. (a) The topology using a TS and two open stubs. (b) The equivalent circuit.*

If the value of Z_{0e}/Z_{0o} in (12) is close to unity, the characteristic-impedance value of Z_T becomes quite large, a concept that can be used for the realization of high-impedance TLs. One implementation of a high-impedance TL is presented in Figure 24(a) and consists of one TS with an electrical length of Θ and two identical open stubs with characteristic impedance of Z_{op} and electrical length of $Θ_{op}$ located at both ends of the TS. The equivalent circuit is shown in Figure 24(b), where the TS in Figure 24(a) is replaced by the TS equivalent circuit in Figure 19(b).

Since both circuits in Figure 24 are symmetric, even- and odd-mode excitation analyses can be used for their design. The even- and odd-mode admittances Y_{ev} and Y_{od} can be expressed as

$$Y_{ev} = j(Y_{op}\tan_{op} - Y_{oe}\cot) - j\frac{Y_{0o} - Y_{0e}}{2}\cot\frac{\Theta}{2}, \quad (13a)$$

$$Y_{od} = j(Y_{op}\tan_{op} - Y_{oe}\cot\Theta) + j\frac{Y_{0o} - Y_{0e}}{2}\tan\frac{\Theta}{2}, \quad (13b)$$

so the reflection coefficients $S_{11} = S_{22}$ of the circuit may be written in terms of the eigenvalues s_1 and s_2, such as

$$S_{11} = S_{22} = \frac{s_1 + s_2}{2} = \frac{Y_0^2 - Y_{ev}Y_{od}}{(Y_0 + Y_{ev})(Y_0 + Y_{od})}, \quad (14)$$

where $s_1 = (Y_0 - Y_{ev})/(Y_0 + Y_{ev})$ and $s_1 = (Y_0 - Y_{od})/(Y_0 + Y_{od})$.

To guarantee a perfect match at both ports, the numerator in (14) needs to be zero, which results in

$$(Y_{op}\tan\Theta_{op} - Y_{oe}\cot\Theta)(Y_{op}\tan\Theta_{op} - Y_{oo}\cot\Theta) = 0. \quad (15)$$

From (15), the two solutions for the parameters of the open stubs can be expressed as

$$\text{Solution 1: } Y_{op} \tan \Theta_{op} = Y_{oe} \cot \Theta, \qquad (16a)$$

$$\text{Solution 2: } Y_{op} \tan \Theta_{op} = Y_{oo} \cot \Theta. \qquad (16b)$$

Based on the two solutions in (16), several high-impedance ($Z_0 = Z_T = 200\,\Omega$) TL implementations using the topology in Figure 24(a) were simulated at the design frequency of 1 GHz for different electrical lengths Θ and a fixed coupling coefficient of $C = -8.5$ dB ($Z_{0e} = 120.4\,\Omega$ and $Z_{0o} = 54.6\,\Omega$). If the electrical length Θ_{op} of the open stubs in Figure 24 was chosen as $90° - \Theta$, the characteristic impedance Z_{op} of the open stubs is the same as the even- or odd-mode impedance, depending on the solutions referring to (16). The frequency responses for solutions 1 and 2 are plotted in Figure 25(a) and (b), respectively. For solution 1 in Figure 25(a), when the electrical length Θ is 90°, the open stubs are not necessary from (16), and perfect matching appears only at 1 GHz. As the electrical lengths gradually decrease from 90°, perfect matching occurs only at 1 GHz regardless of the electrical lengths of Θ, and additional near-perfect match points appear at 1.06, 1.14, and 1.2 GHz for $\Theta = 80°$, $\Theta = 70°$, and $\Theta = 60°$, respectively. For solution 2 in Figure 25(b), the perfect match for all cases is achieved at 1 GHz regardless of the electrical lengths of Θ, and the additional near-perfect matching points appear at 0.89, 0.82, and 0.79 GHz for $\Theta = 80°$, $\Theta = 70°$, and $\Theta = 60°$, respectively. The two frequency responses for the same electrical lengths but for the different solutions 1 and 2, derived using 16(a) and (b), respectively, are not symmetric with respect to 1 GHz. Further, the additional near-perfect matching points with solution 2 are located farther from 1 GHz than those with solution 1. If the bandwidth is defined as the frequency range where $|S_{11}|$ is lower than -15 dB, the bandwidth with $\Theta = 90°$ is 0.85–1.15 GHz (30%), and those with $\Theta = 80°$, 70, and 60° are 0.88–1.19 GHz (31%), 0.9–1.24 GHz (34%), and 0.93–1.27 GHz (34%), respectively, for solution 1 in Figure 25(a). The bandwidths are, therefore, approximately the same with any electrical length of Θ, especially if limited to 60–90°.
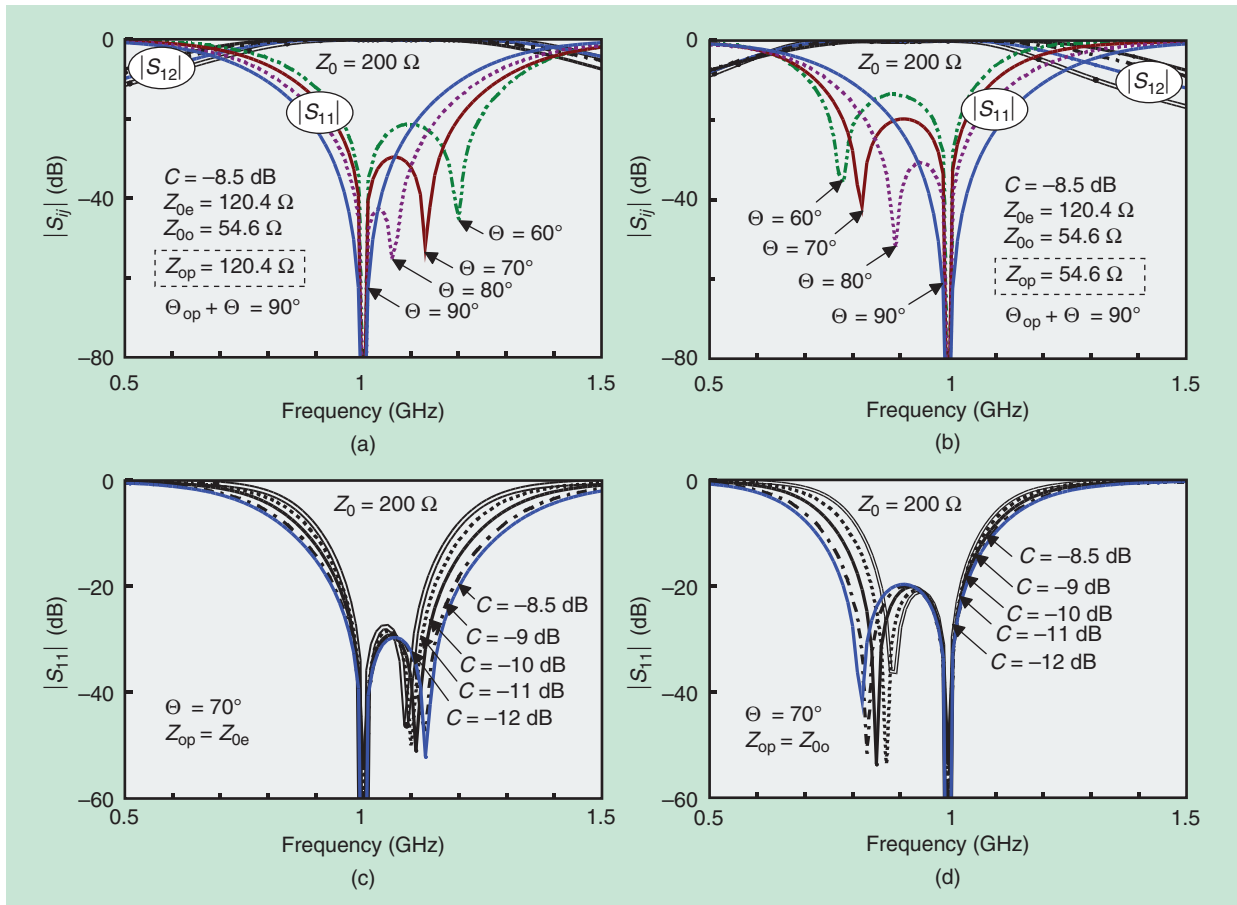

Figure 25. *The simulation results for various implementations of high-impedance (200-Ω) TLs using the proposed topology. (a) $|S_{11}|$ and $|S_{21}|$ for solution 1 for numerous Θ values. (b) $|S_{11}|$ and $|S_{21}|$ for solution 2 for numerous Θ values. (c) $|S_{11}|$ for solution 1 for numerous coupling-coefficient values. (d) $|S_{11}|$ for solution 2 for numerous coupling-coefficient values.*

Even for different values of the coupling coefficients and the same electrical lengths, the frequency responses are roughly the same near the design frequency and different for frequencies away from that. As an example, another set of simulations was carried out at the design frequency of 1 GHz, varying the coupling-coefficient values from −8.5 dB to −12 dB; the scattering-parameter results are shown in Figure 25(c) and (d) for solutions 1 and 2, respectively. For larger values of the coupling coefficient, the bandwidths become wider, and the additional near-perfect points move gradually farther away from the design frequency, resulting in wider bandwidths. The bandwidth with $C = −9$ dB is, therefore, wider than that with $C = −12$ dB. The process of generating additional near-perfect matching points for different values of the coupling coefficients seems to be similar to that with different electrical lengths, although it is clear that the bandwidths are mainly determined by the coupling-coefficient values.

To experimentally verify the performance of the proposed implementation of high-impedance TLs, two stages of quarter-wave impedance transformers to convert 1 KΩ into 50 Ω using the topology shown in Figure 26(a) were created at the design frequency of 3 GHz, and the proof-of-concept prototype was realized on the RT/duroid 5870 substrate ($\varepsilon_r = 2.33$, $h = 0.787$ mm), as shown in Figure 26(b). The first stage transforms 1 KΩ into 700 Ω, and the second converts 700 Ω into 50 Ω. The characteristic impedances of the first and second impedance transformers are, therefore, 836.7 Ω and 187.0 Ω. The even- and odd-mode impedances required for the realization of these characteristic-impedance values are shown in Table 5 for different values of the coupling coefficients using (11).

Since the even-mode impedance is proportional to both the characteristic-impedance values of Z_T and the coupling coefficients of the utilized coupled-line section, as demonstrated in Table 5, the chosen coupling coefficient should be as small as possible to enable an easily realizable even-mode impedance for the matching sections featuring high impedance values. A coupling coefficient for the first stage was chosen as −19 dB for $Z_T = 836.7$ Ω (Table 5). Since the odd-mode impedance is also proportional to the characteristic-impedance values and coupling coefficients, the coupling coefficient for the second stage was chosen as −12 dB for $Z_T = 187.0$ Ω so that the odd-mode impedance was not too small (Table 5). For these design specifications, the fabrication dimensions (width, ω, and gap size, s) of the high-impedance TLs were calculated to be $\omega = 0.7$ mm and $s = 1.17$ mm for the first stage of the impedance transformer and $\omega = 2.13$ mm and $s = 0.2$ mm for the second. The measured and simulated matching $|S_{11}|$ results for the realized prototype are given in Figure 27, demonstrating good agreement and an excellent match (below −39 dB) near 3 GHz.

To show the feasibility of such a high impedance value of $Z_T = 836.7$ Ω, the first-stage impedance transformation was selected as 1 KΩ–700 Ω, requiring a narrow bandwidth due to the low coupling coefficient of −19 dB. However, to enhance the bandwidth, the midpoint between the first and second stages can be selected as $\sqrt{1000 \times 50} = 223$ Ω. The first- and second-stage characteristic impedances are 472.2 Ω and 105.6 Ω, respectively; thus, one of the two does not need to be realized with the TS.

To increase their bandwidths, the impedance transformers can be implemented with a combination of TSs and single TLs. The example presented in Figure 28(a) consists of one TS and one 90° single TL. The characteristic impedance of the single TL is 100 Ω, and the even- and odd-mode impedances Z_{0e} and Z_{0o}
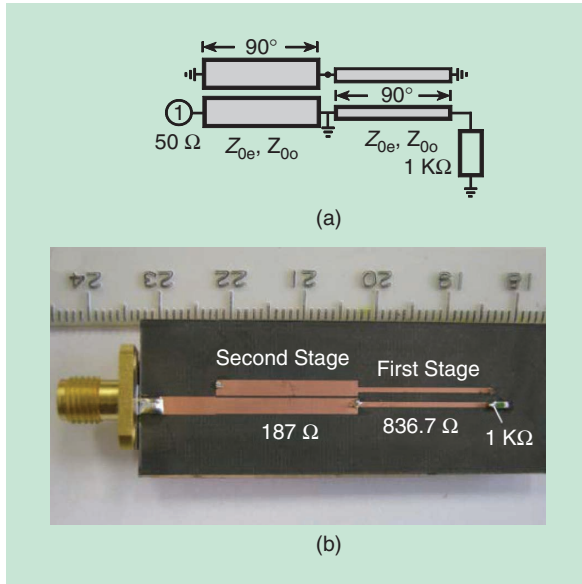

Figure 26. *The impedance transformer from 1 KΩ to 50 Ω. (a) The detailed circuit topology. (b) The fabricated prototype consisting of two CPL impedance-transforming stages (1 KΩ to 700 Ω to 50 Ω).*

TABLE 5. The even- and odd-mode impedances for $Z_T = 836.7$ Ω and $Z_T = 187.0$ Ω.

$Z_T = 836.7$ Ω					
C (dB)	−15	−17	−19	−21	−23
Z_{0e} (Ω)	181	137.6	105.7	81.9	63.7
Z_{0o} (Ω)	126.3	103.6	84.4	68.5	55.3
$w = 0.711$ mm, $s = 1.17$ mm, and $l = 18.5$ mm.					
$Z_T = 187$ (Ω)					
C (dB)	−8	−10	−12	−14	−16
Z_{0e} (Ω)	123.7	86.5	62.8	46.6	35.2
Z_{0o} (Ω)	53.3	44.9	37.6	31.1	25.6
$w = 2.13$ mm, $s = 0.2$ mm, and $l = 18.08$ mm.					

of the TS are 129 Ω and 81.8 Ω, respectively, which is equivalent to the characteristic impedance of 447.2 Ω.

The impedance transformer was designed at 2 GHz and fabricated on a flexible RT/duroid 6002 substrate ($\varepsilon_r = 2.94$, $h = 20$ mil). The fabricated circuit prototype is illustrated in Figure 28(b), and the three impedance transformers in Figure 28(c)–(e) with bending configurations for an increasing curvature show excellent performance in typical wearable-electronics configurations. The measured frequency responses for all four (one unbent and three bending configurations) are compared in Figure 29, with the simulated and measured frequency responses of the unbent one in Figure 28(b) expressed as dotted and solid lines, respectively, while those of three bending ones in Figure 28(c)–(e) are shown with different symbols. From the figure, the bandwidths of the impedance transformers in Figure 28(a) are generally wider than those with two TSs in Figure 27, and a very good agreement between the measured and simulated responses is clearly demonstrated. The frequency responses feature a slight shift depending on the curvatures, but all are acceptable. Therefore, it can be concluded that the theory suggested so far can be applied to a variety of wearable and flexible environments. Because of the performance of these TS-based implementations of high-impedance TLs, these structures can be used, as well, for the implementation of CRHs and power dividers with arbitrarily high power-division ratios, to be discussed in the following sections.

CRHs With High Power-Division Ratios

The TS-based implementation of the CRH shown in Figure 20(b) would require $Z_1 = Z_3 = 52.44$ Ω and $Z_2 = Z_4 = 165.83$ Ω to achieve a power-division ratio of 10 dB [32]. To implement the 270° TL with Z_4 in a miniaturized way, the TS topology of Figure 19(a) with $\Theta = 90°$ can be easily used. For the implementation of the short 90° TL featuring the characteristic impedan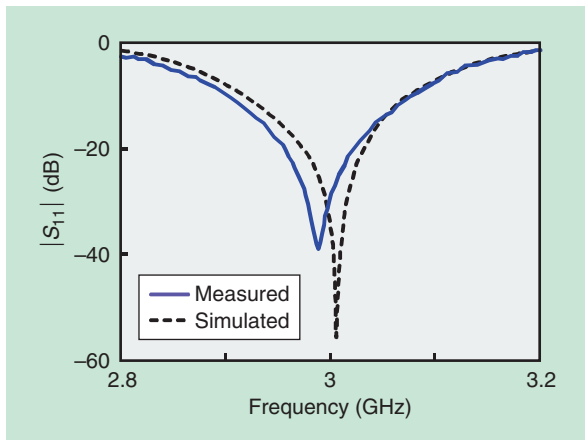ce Z_2 in microstrip technologies, three possible topologies (L_{S1}-, L_{S2}-, and ML_{S2}-type) that combine TLs with inductors can be used, as shown in Table 6.

The L_{S1}-type consists of two identical TLs and an inductor, while the L_{S2}-type is composed of two identical inductors and one TL. Since the two inductors are located at both ends of the L_{S2}-type section, they could pose a practical issue for the implementation of four-port geometries; therefore, a modified form (ML_{S2}-type) is necessary. The ML_{S2}-type incorporates three TLs, two of which are identical, and two identical inductors. Two fabricated ring-hybrid prototypes for power-division ratios of 13 and 11 dB are illustrated in Figure 30(a) and (b), respectively, where $N = 2$ stages of the L_{S1}-type (13 dB) and $N = 1$ stage
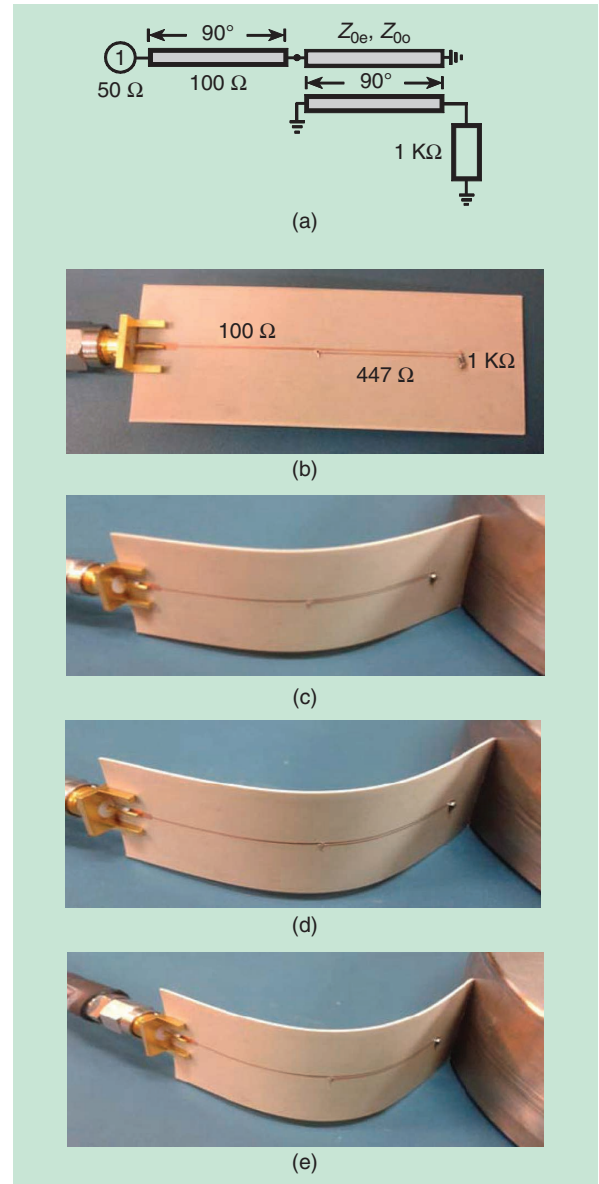

Figure 28. *The impedance transformers. (a) The detailed circuit topology. (b) The circuit prototype (no bending). (c)–(e) The bending configurations for an increasing curvature.*

Figure 27. *The measured and simulated $|S_{11}|$ values for the prototype shown in Figure 26(b).*

L_{S1}-type	L_{S2}-type	ML_{S2}-type
$Z_{L_{S1}} = Z_h \dfrac{\tan(\Theta_{L_{S1}}/2)}{\tan(\Theta_h/2)}$	$Z_{L_{S2}} = Z_h \dfrac{\sin\Theta_{L_{S2}}}{\sin\Theta_h}$	$Z_{ML_{S2}} = Z_Q \dfrac{\sin\Theta_{ML_{S2}}}{\sin\Theta_Q}$
$\omega L_{S1} = 2 Z_h \dfrac{\tan^2\frac{\Theta_h}{2} - \tan^2\frac{\Theta_{L_{S1}}}{2}}{\tan\frac{\Theta_h}{2} + \tan^3\frac{\Theta_h}{2}}$	$\omega L_{S2} = Z_0 \dfrac{\cos\Theta_{L_{S2}} - \cos\Theta_h}{\sin\Theta_h}$	$\omega ML_{S2} = Z_Q \dfrac{\cos\Theta_{ML_{S2}} - \cos\Theta_Q}{\sin\Theta_Q}$

For the ML_{S2}-type, Z_Q and Θ_Q are given by

$$Z_Q = Z_P \sqrt{\left(\frac{Z_h \cot\frac{\Theta_h}{2} + Z_P \tan\Theta_P}{Z_P - Z_h \cot\frac{\Theta_h}{2} \times \tan\Theta_P}\right)\left(\frac{Z_h \tan\frac{\Theta_h}{2} - Z_P \tan\Theta_P}{Z_h \tan\frac{\Theta_h}{2} \times \tan\Theta_P + Z_P}\right)},$$

$$\tan\frac{\Theta_Q}{2} = \sqrt{\left(\frac{Z_P - Z_h \cot\frac{\Theta_h}{2} \times \tan\Theta_P}{Z_P + Z_h \tan\frac{\Theta_h}{2} \times \Theta \tan\Theta_P}\right)\left(\frac{Z_h \tan\frac{\Theta_h}{2} - Z_P \tan\Theta_P}{Z_h \cot\frac{\Theta_h}{2} + Z_P \tan\Theta_P}\right)}.$$
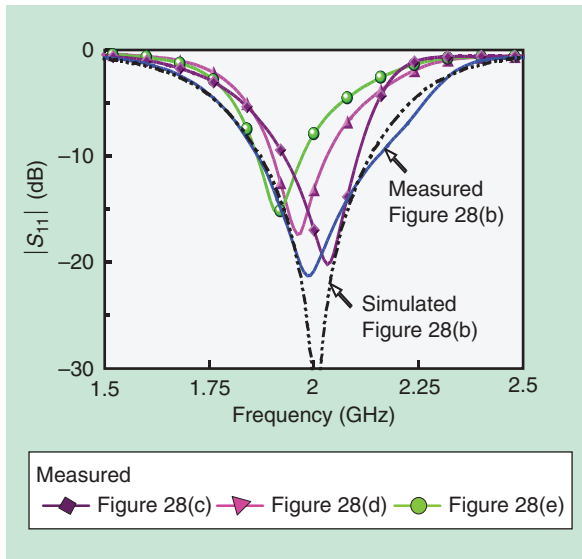

Figure 29. *The measured and simulated frequency responses of the impedance transformers from Figure 28 for different bending configurations.*

of the ML_{S2}-type (11 dB) were fabricated to realize the 90° high-impedance (Z_2) TLs, while the TS stages were used for the implementation of the 270° high-impedance (Z_4) TLs.

The 13-dB ring hybrid was designed at 2 GHz, and its measured and simulated frequency responses are plotted in Figure 31, where the power-division responses are shown in Figure 31(a), isolations in Figure 31(b), matching responses in Figure 31(c), and phase responses in Figure 31(d). Since the ring hybrid in Figure 31(a) was designed for the power-division ratio of 13 dB, the scattering parameter $|S_{41}|$ is calculated as −13.21 dB. Due to the difference of 13 dB between $|S_{21}|$ and $|S_{41}|$, the scattering parameter $|S_{21}|$ is −0.21 dB. The measured $|S_{21}|$ and $|S_{41}|$ are −13.73 and −0.25 dB at 2 GHz, leading to a measured power-division ratio of 13.49 dB. In Figure 31(b), the isolations of $|S_{31}|$ and $|S_{24}|$ at 2 GHz are greater than 40 dB and, overall, greater than 15 dB from 0 to 3.2 GHz. Since the simulated matching results at all ports have similar responses, they are expressed with a single dotted line in Figure 31(c), where the measured return losses at all ports are greater than 20 dB at 2 GHz, and the bandwidth of at least 15 dB of return loss is 1.15–2.9 GHz. The fact that the 13-dB ring hybrid achieves the target isolation, as shown in Figure 31(b), indicates that good in- and out-of-phase responses are possible. The measured phase differences $|\angle S_{21} - \angle S_{41}|$ and $|\angle S_{23} - \angle S_{43}|$ in Figure 31(d) are obtained as 178.9 and 0.244° at 2 GHz, respectively. The measured results are in good agreement with the predicted ones.

The 11-dB ring hybrid in Figure 30(b) was designed at 3 GHz: the measured and predicted results are compared in Figure 32, with power-division responses shown in Figure 32(a), isolations in Figure 32(b), matching responses in Figure 32(c), and phase responses in

Figure 32(d). The measured power-division ratio is 11.26 dB in Figure 32(a), the measured isolations are more than 15 dB above the frequency range of 1.5–4.5 GHz in Figure 32(b), and the return losses at all ports are more than 18 dB in the frequency range of 1.5–3.5 GHz in Figure 32(c). The measured bandwidth of the phase difference $|\angle S_{21} - \angle S_{41}|$ for 180° ±5° is 2.45–3.26 GHz, while those of $|\angle S_{23} - \angle S_{43}|$ for ±5° are 2.62–3.42 GHz in Figure 32(d). The measured results, in general, agree with the predicted ones, given fabrication errors.

Compact CRH With High Power-Division Ratios

Numerous multifunctional wireless modules require a substantial reduction in mass and volume, so the compactness of ring hybrids has been of significant interest [19]. The typical ring-hybrid topology consists of three 90° TLs and one 270° TL. If the power-division ratios are not 0 dB for the same termination impedances Z_0, as shown in Figure 33(a),

two TLs with characteristic impedance Z_1 should be identical, and the other two with characteristic impedance Z_2 should have the same characteristic impedances, for an electrical length difference of 180°. If the power-division ratio is 12 dB with a termination impedance of 50 Ω, the characteristic impedances Z_1 and Z_2 of the TLs should be 51.56 and 205.24 Ω, respectively, and all of the TLs should be as short as possible due to size requirements. However, the TLs with characteristic
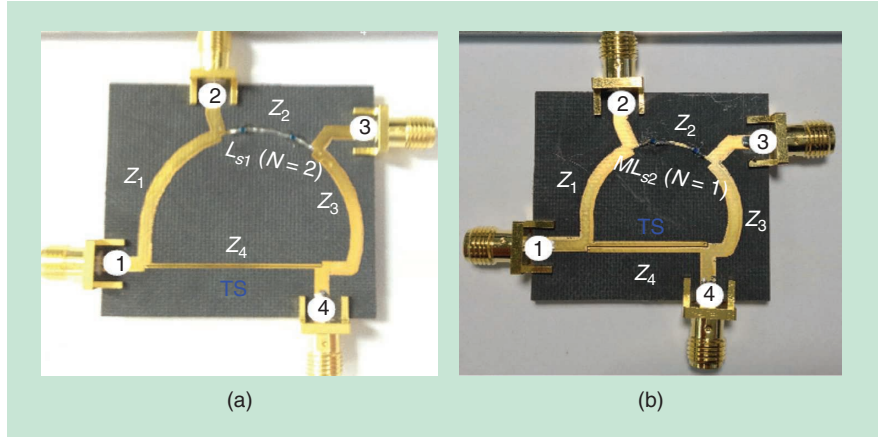

Figure 30. *The fabricated ring hybrids with high power-division ratios [32]. (a) The power-division ratio of 13 dB. (b) The power-division ratio of 11 dB.*
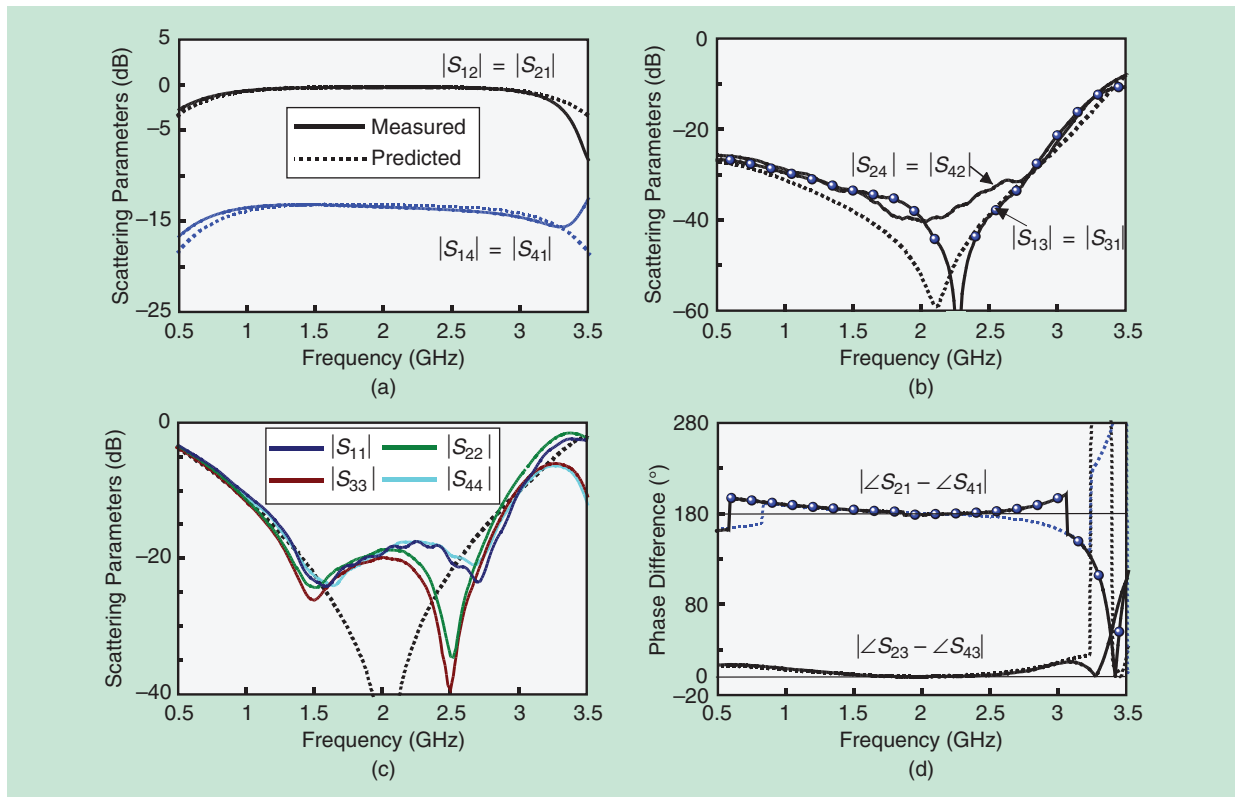

Figure 31. *The measured and simulated frequency responses for the ring hybrid with the 13-dB power-division ratio in Figure 22(a). (a) The power divisions, (b) isolations, (c) matching, and (d) phase responses.*

impedance of 205.24 Ω do not seem to be easy to fabricate with a microstrip technology due to a required width of approximately 40 μm for commonly used substrates (for example, for the prototype discussed in this article, the required microstrip linewidth was 42 μm for a substrate with a thickness of 20 mil and a dielectric constant of 2.2), while the physical length of the low-impedance (51.26-Ω) TLs should be reduced without a significant bandwidth compromise.

Due to the implementation difficulties, most previously reported efforts have investigated compact ring hybrids for equal power divisions and power-division ratios lower than or equal to 6 dB [49]. In [50], high power-division ratios were treated, but the size of the circuits is not compact, and the demanded power-division ratio is achieved only near the design frequency. In [51], a 12-dB power-division ratio was studied, and equivalent/artificial lumped-element TL models were suggested for high-impedance TLs. However, the extraction method for the lumped-element values seems to be very complicated, and the bandwidth is much smaller than that of the conventional one, while the size is not compact. A power-division ratio of 13 dB is investigated in Figure 30(b) [32], but the size (320.58°) is also not compact.

In [19], a novel compact wideband ring hybrid enabling the realization of arbitrarily high power-division ratios in a miniaturized form factor is introduced. In the preliminary ring design for a 12-dB power-division-ratio prototype, the circuit includes two high-impedance TLs with $Z_2 = 205.24$ Ω and two low-impedance 90° TLs with $Z_1 = 51.26$ Ω, as mentioned previously, with each TL being as small as possible. The size-reduction approach should be different for every TL, and conventional methods (such as the T- and Π-types, as in [38] and Figure 6 with $N = 1$) cannot be applied for high-impedance TLs due to their inherent lack of a method to reduce high-impedance values to easier-to-realize lower ones.

Figure 33(b)–(d) presents various compact topologies that effectively realize the 90° and 270° electrical lengths, although their physical lengths correspond to electrical lengths much shorter than 90°. The low-impedance (Z_1) TL with an electrical length of 90°/N_T (N_T: arbitrary integer) in Figure 33(b) can be shortened with the MT-unit block consisting of two identical TLs with characteristic impedance of Z_T and electrical length of $\Theta_T/2$ and two identical shunt stubs with individual susceptance of $S_T/2$ in between. The 270° TL with high impedance of Z_2 in Figure 33(c) can be
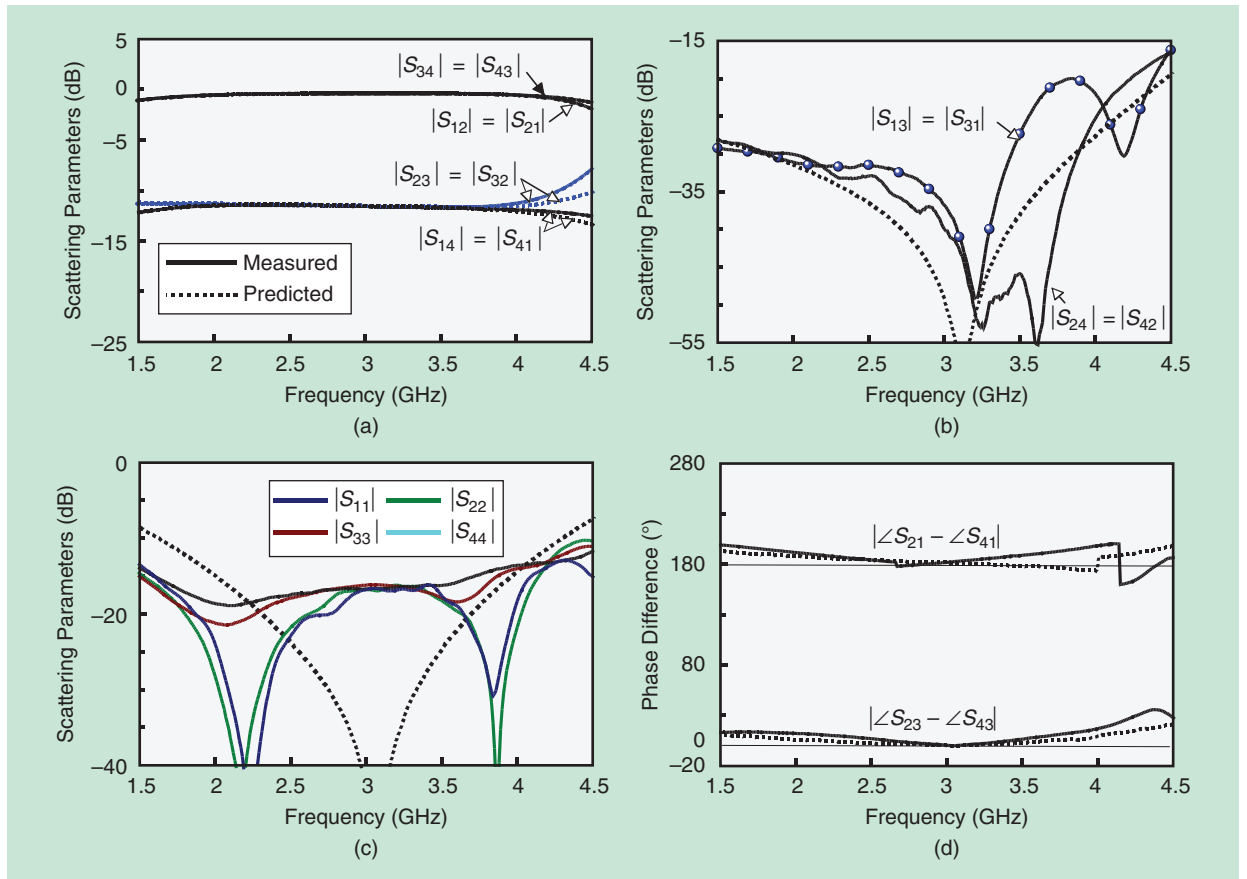

Figure 32. *The measured and simulated frequency responses for the ring hybrid with the 11-dB power-division ratio in Figure 22(b). (a) The power divisions, (b) isolations, (c) matching, and (d) phase responses.*
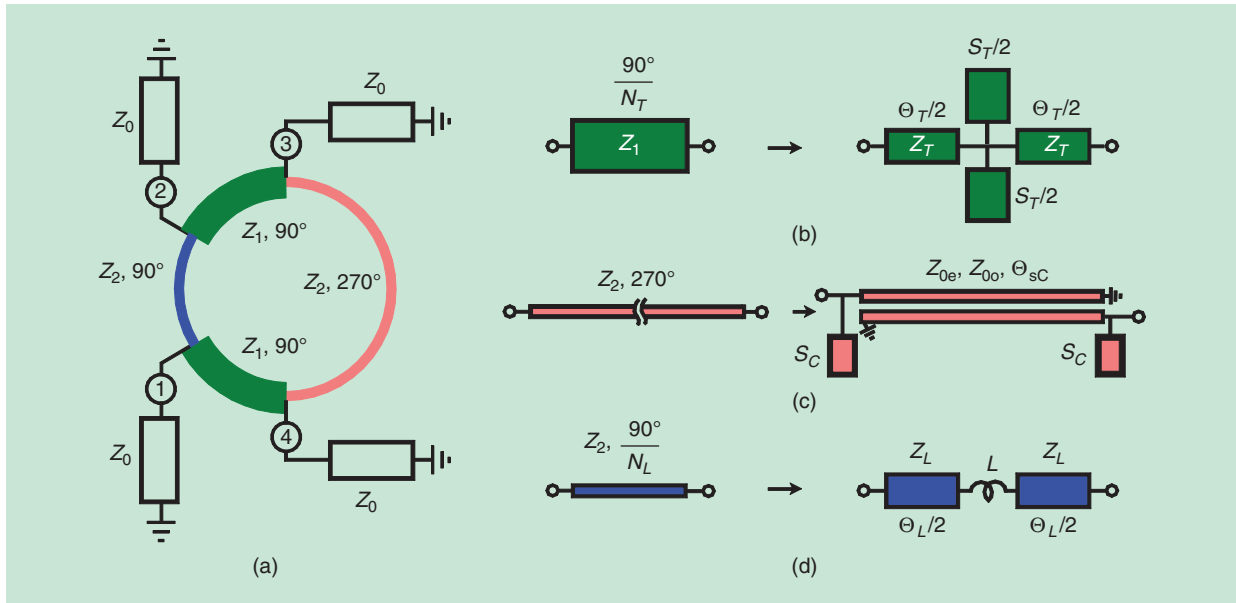
Figure 33. *A ring hybrid and its miniaturization equivalent circuits. (a) The ring hybrid. (b) The MT-unit block for a (90°/N_T) low-impedance (Z_1) TL. (c) The CΠ-section type for a 270° high-impedance (Z_2) TL. (d) The L_{S1}-unit block for a (90°/N_L) high-impedance (Z_2) TL.*

miniaturized using a CPL with even- and odd-mode impedances of Z_{0e} and Z_{0o}, electrical length of Θ_{sC}, and two-shunt open stubs. The electrical length of Θ_{sC} is much shorter than 90°, and the susceptance of each open stub is denoted as S_C. The equivalent circuit in Figure 33(c) is named the coupled-line Π-section (CΠ) type. The high-impedance (Z_2) TL with an electrical length of 90°/N_L (N_L: arbitrary integer) in Figure 33(d) can be miniaturized, with the L_{S1}-unit block composed of two identical TLs with Z_L and $\Theta_L/2$ interconnected with one series inductance, L. The integers N_T and N_L of the MT- and L_{S1}-section unit cells are typically smaller than five and represent the number of unit cells required to effectively realize the aggregate electrical lengths of 90° for the low- and high -impedance TLs, respectively.

Using the miniaturized equivalent circuits, the ring hybrid in Figure 33(a) can be reduced, and a fabricated compact CRH with a power-division ratio of 12 dB is shown in Figure 34, where low-impedance TLs are fabricated using the MT-unit block with $N = 3$ in Figure 33(b), while 270° and 90° high-impedance TLs are implemented with the CΠ-section type in Figure 33(c) and the L_{S1}-unit block with $N = 2$ in Figure 33(d), respectively.

The circumference of the fabricated prototype in Figure 34 is only 209.3° long, compared to 540° for conventional implementations, verifying an area miniaturization down to 15%, while the measured bandwidth of the 15-dB return loss is 78% versus the conventional approach's 44%, an improvement by a factor 1.8. The topology in Figure 34, introduced in [19], could be easily optimized for a wide range of power-division ratios
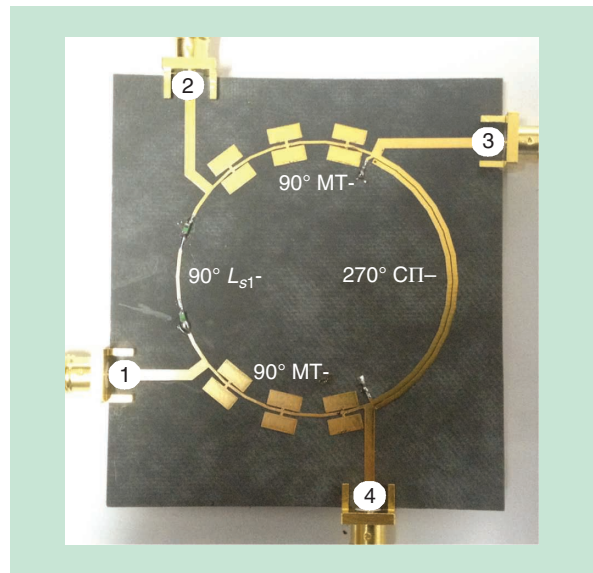

Figure 34. *The fabricated compact CRH [19].*

and set the foundation for the implementation of similar ultraminiaturized CRHs in a variety of wearable and flexible applications.

Three-Port Power Dividers and Branch-Line Hybrids With High Power-Division Ratios

The TS topologies reviewed in the previous sections can be also used for the fabrication of Wilkinson power dividers [43] and branch-line hybrids [44] with arbitrarily high power-division ratios. A typical Wilkinson power divider consists of two TLs with lengths of 90° or 270°. To achieve a 10-dB power-division ratio, one of the
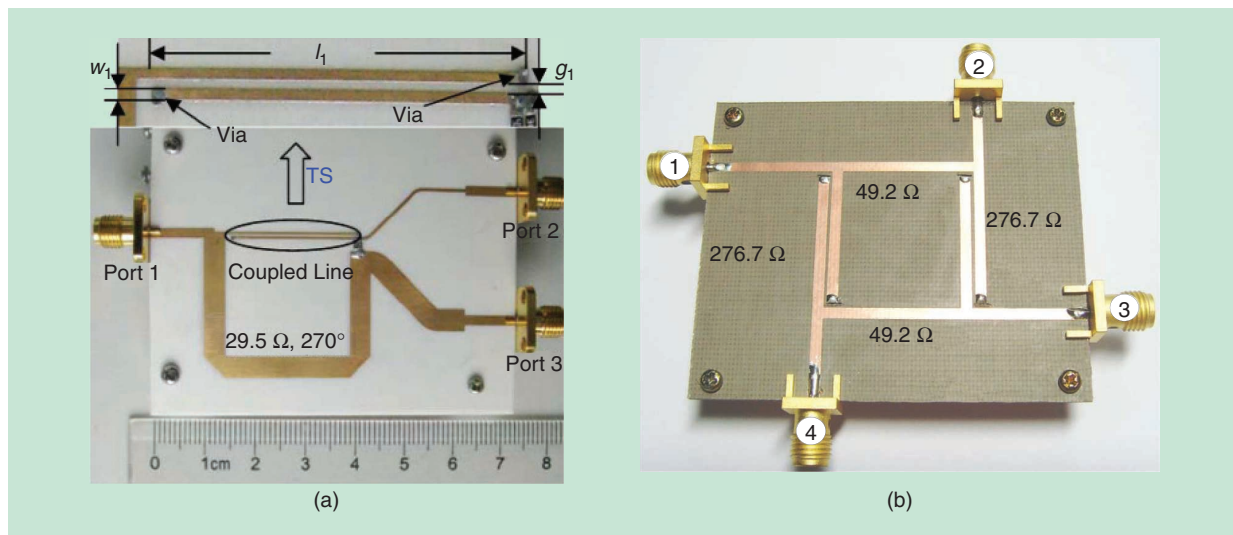
Figure 35. *The high-division-ratio power-divider prototypes using TSs. (a) The Wilkinson power divider with a power-division ratio of 10 dB [43]. (b) The branch-line hybrid with a power-division ratio of 15 dB [44].*

two TLs should feature a high impedance of 294.9 Ω, which can be implemented using one TS, as shown in the fabricated prototype in Figure 35(a).

Similarly, a typical branch-line hybrid consists of four 90° TLs or two 90° TLs and two 270° TLs. If the termination impedances are the same, the two sets of TLs located in parallel (for example, the left and right side) should be identical. To achieve a power-division ratio of 15 dB for the same termination resistance of 50 Ω, two sets of TLs with characteristic impedances of 49.2 Ω and 276.69 Ω are required. For the miniaturized fabrication of the two TLs with a 276.69-Ω characteristic impedance, the TSs can be implemented as shown in Figure 35(b).

Conclusions

This article introduced design formulas for three equivalent circuits for a directional coupler and two-port coupled line sections (TO and TS) that can be used as versatile building blocks for a variety of RF components commonly used in wearable and flexible applications. The proposed equivalent circuits for the directional coupler feature uncoupled TLs with a wide band and compact sizes; therefore, Marchand baluns can be fabricated easily in planar structures with any connecting segment. TO and TS structures can be simply realized by terminating two diagonal ports of a directional coupler in open/short circuits, and they feature unique properties compared to single TL sections, such as a miniaturized length, 180° phase shift, easy planar realization of very high characteristic-impedance values, and dc blocking.

Since design formulas for such structures have been reported in the past for only a −3-dB coupling coefficient, modified design formulas were introduced for arbitrary power coupling ratios, which enhance their applicability to applications with stringent electromagnetic interference/electromagnetic compatibility, bandwidth, and size limitations. Various examples confirming the excellent performance of the TO/TS sections were discussed. The TS-inherent 180° phase shift enables the realization of miniaturized enhanced-bandwidth ring hybrids, while the effective realization of high impedance values facilitates the design and fabrication of power dividers with arbitrarily high power division ratios, which were previously considered too difficult to realize, and sets the foundation for power dividers in wearable and flexible RF electronics.

References
[1] J. G. D. Hester, J. Kimionis, and M. M. Tentzeris, "Printed motes for IoT wireless networks: State of the art, challenges, and outlooks," *IEEE Trans. Microw. Theory Techn.*, vol. 65, no. 5, pp. 1819–1830, May 2017.
[2] S. B. Cohn and R. Levy, "History of microwave passive components with particular attention to directional couplers," *IEEE Trans. Microw. Theory Techn.*, vol. MTT-32, no. 9, pp. 1046–1054, Sept. 1984.
[3] E. M. T. Jones and J. T. Bolljahn, "Coupled-strip-transmission-line filters and directional couplers," *IRE Trans. Microw. Theory Techn.*, vol. MTT-4, no. 2, pp. 75–81, Apr. 1956.
[4] S. B. Cohn, "Parallel-coupled transmission-line-resonators filters," *IRE Trans. Microw. Theory Techn.*, vol. MTT-6, no. 2, pp. 223–231, Apr. 1958.
[5] G. L. Matthaei, "Interdigital band-pass filters," *IRE Trans. Microw. Theory Techn.*, vol. MTT-10, no. 6, pp. 479–491, Nov. 1962.
[6] R. Levy, "General synthesis of asymmetric multi-element coupled transmission line directional couplers," *IEEE Trans. Microw. Theory Techn.*, vol. MTT-11, no. 4, pp. 226–237, July 1963.
[7] E. G. Cristal, "Coupled-transmission: Line directional couplers with coupled lines of unequal characteristic impedances," *IEEE Trans. Microw. Theory Techn.*, vol. MTT-14, no. 7, pp. 337–346, July 1966.
[8] J. P. Shelton, "Impedances of offset parallel-coupled strip transmission lines," *IEEE Trans. Microw. Theory Techn.*, vol. MTT-14, no. 1, pp. 7–15, Jan. 1966.
[9] G. I. Zysman and A. K. Johnson, "Coupled transmission line networks in an inhomogeneous dielectric medium," *IEEE Trans. Microw. Theory Techn.*, vol. MTT-17, no. 10, pp. 753–759, Oct. 1969.

[10] M. K. Krage and G. I. Haddad, "Characteristics of coupled microstrip transmission lines-I: Coupled-mode formulation of inhomogeneous lines," *IEEE Trans. Microw. Theory Techn.*, vol. MTT-18, no. 4, pp. 217–222, Apr. 1970.

[11] W. Ou, "Design equations for an interdigitated directional coupler," *IEEE Trans. Microw. Theory Techn.*, vol. MTT-23, no. 2, pp. 253–255, Feb. 1975.

[12] V. J. Tripathi, "Asymmetric coupled transmission lines in an inhomogeneous medium," *IEEE Trans. Microw. Theory Techn.*, vol. MTT-23, no. 9, pp. 734–739, Sept. 1975.

[13] J. Mueller, M. N. Pham, and A. F. Jacob, "Directional coupler compensation with optimally positioned capacitances," *IEEE Trans. Microw. Theory Techn.*, vol. 59, no. 11, pp. 2824–2832, Nov. 2011.

[14] H.-R. Ahn and B. Kim, "Transmission-line directional couplers for impedance transforming," *IEEE Microw. Compon. Lett.*, vol. 16, no. 10, pp. 537–539, Oct. 2006.

[15] K.-X. Wang, X. Y. Zhang, and B.-J. Hu, "Gysel power divider with arbitrary power ratios and filtering responses using coupling structure," *IEEE Trans. Microw. Theory Techn.*, vol. 62, no. 3, pp. 431–440, Mar. 2014.

[16] S. Chen, Y. Yu, and M. Tang, "Planar out-of-phase Gysel power divider with high power splitting ratio," *Electron. Lett.*, vol. 51, no. 24, pp. 2010–2012, 2015.

[17] Y. Konishi, I. Awai, Y. Fukuoka, and M. Nakajima, "A directional coupler of a vertically installed planar circuit structure," *IEEE Trans. Microw. Theory Techn.*, vol. 36, no. 6, pp. 1057–1063, June 1988.

[18] H.-R. Ahn and M. M. Tentzeris, "Novel generic asymmetric and symmetric equivalent circuits of 90° coupled-line sections applicable to any Marchand balun," *IEEE Trans. Microw. Theory Techn.*, vol. 65, no. 3, pp. 746–760, Mar. 2017.

[19] H.-R. Ahn and M. M. Tentzeris, "A novel wideband, compact, microstrip coupled-line ring hybrid for arbitrarily high power-division ratios," *IEEE Trans. Circuit Syst. II, Exp. Briefs*, vol. 64, no. 6, pp. 630–634, June 2017.

[20] H.-R. Ahn and M. M. Tentzeris, "Wideband and compact impedance-transforming 90° DC blocks with symmetric coupled transmission-line sections," *IEEE Trans. Compon., Packag. Manuf. Technol.*, vol. 9, no. 1, pp. 80–87, Jan. 2019.

[21] S. R. Borgaonkar and S. N. Rao, "Analysis and design of DC blocks," *Electron. Lett.*, vol. 17, no. 2, pp. 101–103, Jan. 1981.

[22] S.-H. Choi, J.-Y. Lee, K.-B. Lee, and D.-H. Shin, "Design of miniaturized symmetric microstrip DC block," in *Proc. 2007 Asia-Pacific Microwave Conf. (APMC)*.

[23] B. Strassner and K. Chang, "New wide-band DC block cymbal bandpass filter," *IEEE Trans. Microw. Theory Techn.*, vol. 50, no. 5, pp. 1431–1432, May 2002.

[24] S. Lee and Y. Lee, "Generalized miniaturization method for coupled-line bandpass filters by reactive loading," *IEEE Trans. Microw. Theory Techn.*, vol. 58, no. 9, pp. 2383–2391, Sept. 2010.

[25] B. Kim, S. Nam, H.-R. Ahn, and J.-H. Song, "Design of wideband coupled line DC block with compact size," *IEICE Trans. Electron.*, vol. E97-C, no. 9, pp. 915–917, Sept. 2014.

[26] W. Zhao, Y. Zhang, M. Zhan, L. Li, S. Liu, and R. Xu, "Compact broadband DC-block filter," in *Proc. IEEE Int. Conf. Communication Problem-Solving*, 2014, pp. 439–441.

[27] H.-R. Ahn and S. Nam, "Wideband coupled-line microstrip filters with high-impedance short-circuited stubs," *IEEE Microw. Compon. Lett.*, vol. 21, no. 11, pp. 586–588, Nov. 2011.

[28] S. March, "A wideband stripline hybrid ring," *IEEE Trans. Microw. Theory Techn.*, vol. MTT-16, no. 6, pp. 361–362, June 1968.

[29] H.-R. Ahn, I. Wolff, and I-S. Chang, "Arbitrary termination impedances, arbitrary power division, and small-sized ring hybrids," *IEEE Trans. Microw. Theory Techn.*, vol. 45, pp. 2241–2247, Dec. 1997.

[30] H.-R. Ahn and B. Kim, "Small wideband coupled-line ring hybrids with no restriction on coupling power," *IEEE Trans. Microw. Theory Techn.*, vol. 57, no. 7, pp. 1806–1817, July 2009.

[31] H.-R. Ahn and S. Nam, "Compact microstrip 3-dB coupled-line ring and branch-line hybrids with new symmetric equivalent circuits," *IEEE Trans. Microw. Theory Techn.*, vol. 61, no. 3, pp. 1067–1077, Mar. 2013.

[32] H.-R. Ahn and S. Nam, "Wideband microstrip coupled-line ring hybrids for high power-division ratios," *IEEE Trans. Microw. Theory Techn.*, vol. 61, no. 5, pp. 1768–1780, May 2013.

[33] H.-R. Ahn and T. Itoh, "Impedance-transforming symmetric and asymmetric DC blocks," *IEEE Trans. Microw. Theory Techn.*, vol. 58, no. 9, pp. 2463–2474, Sept. 2010.

[34] H.-R. Ahn and T. Itoh, "Corrections to 'impedance-transforming symmetric and asymmetric DC blocks'," *IEEE Trans. Microw. Theory Techn.*, vol. 59, no. 1, p. 207, Jan. 2011.

[35] D. Kajfez and B. S. Vidula, "Design equations for symmetric microstrip DC blocks," *IEEE Trans. Microw. Theory Techn.*, vol. MTT-28, no. 9, pp. 974–981, Sept. 1980.

[36] A. Podcameni, "Symmetrical and asymmetrical edge-coupled-line impedance transformers with a prescribed insertion loss design," *IEEE Trans. Microw. Theory Techn.*, vol. MTT-34, no. 1, pp. 1–7, Jan. 1986.

[37] N. Marchand, "Transmission line conversion transformers," *Electronics*, vol. 17, no. 12, pp. 142–145, Dec. 1944.

[38] H.-R. Ahn and S. Nam, "New design formulas for impedance-transforming 3-dB Marchand baluns," *IEEE Trans. Microw. Theory Techn.*, vol. 59, no. 11, pp. 2816–2823, Nov. 2011.

[39] A. C. Chen, A.-V. Pham, and R. E. Leoni, III, "A novel broadband even-mode matching network for Marchand baluns," *IEEE Trans. Microw. Theory Techn.*, vol. 57, no. 12, pp. 2973–2980, Dec. 2009.

[40] C.-S. Lien, C.-H. Wang, C.-S. Lin, P.-S. Wu, K.-Y. Lin, and H. Wang, "Analysis and design of reduced-size Marchand rat-race hybrid for millimeter-wave compact balanced mixers in 130-nm CMOS process," *IEEE Trans. Microw. Theory Techn.*, vol. 57, no. 8, pp. 1966–1977, Aug. 2009.

[41] Z. Xu and L. NaceEachern, "Optimum design of wideband compensated and uncompendated Marchand baluns with step transformers," *IEEE Trans. Microw. Theory Techn.*, vol. 57, no. 8, pp. 2064–2071, Aug. 2009.

[42] Q. S. Wu and L. Zhu, "Short-ended coupled-line impedance transformers with ultrahigh transforming ratio and bandpass selectivity suitable for large load impedances," *IEEE Trans. Compon. Packag. Manuf. Technol.*, vol. 6, no. 5, pp. 767–774, May 2016.

[43] B. Li, X. Wu, and W. Wu, "A 10: 1 unequal Wilkinson power divider using coupled lines with two shorts," *IEEE Microw. Wireless Compon. Lett.*, vol. 19, no. 12, pp. 789–791, Dec. 2009.

[44] H. R. Ahn, J. Kim, and B. Kim, "Branch-line hybrids with -15 dB coupling power," in *Proc. Asia Pacific Microwave Conf. (APMC 2008)*, B1-3 Paper, Hong Kong, 2008.

[45] H.-R. Ahn and B. Kim, "Equivalent transmission-line sections for very high impedances and their application to branch-line hybrids with very weak coupling power," *J. Korea Inst. Electromag. Eng. Sci.*, vol. 9, no. 2, pp. 85–97, June 2009.

[46] G. L. Matthaei, L. Young, and E. M. T. Jones, *Microwave Filter, Impedance-Matching Networks, and Coupling Structures*. Norwood, MA: Artech House, 1980, pp. 219–228.

[47] H.-R. Ahn and S. Nam, "Design method for Butter-Cheby bandpass filters with even number of resonators," *IEEE Trans. Microw. Theory Techn.*, vol. 60, no. 6, pp. 1549–1559, June 2012.

[48] H.-R. Ahn, "Reply to 'comments on reply to comments on wideband coupled-line filters with high-impedance short-circuited stubs'," *IEEE Microw. Wireless Compon. Lett.*, vol. 24, no. 5, pp. 357–359, May 2014.

[49] C.-L. Hsu, J.-T. Kuo, and C.-W. Chang, "Miniaturized dual-band hybrid couplers with arbitrary power division ratios," *IEEE Trans. Microw. Theory Techn.*, vol. 57, no. 1, pp. 149–156, Jan. 2009.

[50] M.-J. Park and B. Lee, "Design of ring couplers for arbitrary power division with 50 Ω lines," *IEEE Microw. Wireless Compon. Lett.*, vol. 21, no. 4, pp. 185–187, Apr. 2011.

[51] K.-L. Ho and P.-L. Chi, "Miniaturized and large-division-ratio ring coupler using novel transmission-line elements," *IEEE Microw. Wireless Compon. Lett.*, vol. 24, no. 1, pp. 35–37, Jan. 2014.